A&A, 688, A28 (2024)
https://doi.org/10.1051/0004-6361/202348185

Astronomy & Astrophysics

Extreme-emission-line galaxies in the MUSE *Hubble* Ultra Deep Field Survey

I. del Moral-Castro[1,2,3], J. M. Vílchez[4], J. Iglesias-Páramo[4,5], and A. Arroyo-Polonio[4]

[1] Instituto de Astrofísica, Facultad de Física, Pontificia Universidad Católica de Chile, Campus San Joaquín, Av. Vicuña Mackenna 4860, Macul, Santiago 7820436, Chile
e-mail: ignaciodelmoralcastro.astro@gmail.com
[2] Kapteyn Astronomical Institute, University of Groningen, PO Box 800, 9700 AV Groningen, The Netherlands
[3] Facultad de Física, Universidad de La Laguna, Avda. Astrofísico Fco. Sánchez s/n, 38200 La Laguna, Tenerife, Spain
[4] Instituto de Astrofísica de Andalucía – CSIC, Glorieta de la Astronomía s/n, 18008 Granada, Spain
[5] Centro Astronómico Hispano en Andalucía, Observatorio de Calar Alto, Sierra de los Filabres, 04550 Gérgal, Spain

Received 6 October 2023 / Accepted 7 April 2024

ABSTRACT

Aims. We aim to apply a methodology to build a sample of extreme-emission-line galaxies (EELGs) using integral field spectroscopy data. In this work, we followed the spectroscopic criteria corresponding to EELG selection and used the MUSE *Hubble* Ultra-Deep Field Survey, which includes the deepest spectroscopic survey ever performed.

Methods. Objects in the primary (extended) sample were detected requiring a rest-frame equivalent width of EWo ⩾300 Å (200 Å ≤ EWo ≤ 300 Å) in any of the emission lines of [O II]$\lambda\lambda$3726, 7329, [O III]$\lambda\lambda$5007, 4959, or Hα. A detailed closer inspection of the spectra of the candidates selected has been performed on a one-by-one basis in order to confirm their classification. For this sample, the line fluxes, physical properties, and chemical abundances of the EELGs have been derived, as well as their spatially resolved structure and kinematics.

Results. Four (five) of the galaxies in the primary (extended) sample, ∼57% (∼83%), were spatially resolved. Three (none) of them present a clear pattern compatible with rotation. We show how our entire EELG sample shares the same loci defined by high-redshift galaxies ($z \approx 6$–8) for the mass-metallicity relation, illustrating their role as local analogs.

Key words. galaxies: evolution – galaxies: starburst – galaxies: star formation

1. Introduction

Galaxies hosting strong events of star formation can provide keys to our understanding of early galaxy evolution, since such extreme star-forming objects are expected to be more frequent toward the first epochs of the Universe. In this sense, these highly star-forming galaxies provide useful windows to the high-z Universe, allowing us to study the photon budget required for its reionization (e.g. Stark 2016; Dayal & Ferrara 2018). The nature, properties and prevalence of these galaxies at the Epoch of Reionization (EoR) remain to be fully understood.

All these galaxies have been named, as a class, as extreme-emission-line galaxies (EELGs) since their (optical) spectra show very strong emission lines with extreme equivalent width (EW). EELGs host a considerable number of massive, young, star-forming systems producing a substantial amount of photoionizing radiation. This radiation is absorbed by the surrounding metal-poor gas (e.g., Ravindranath et al. 2020). Since the gas is expected to have a perforated irregular distribution, hard ionizing radiation could escape (e.g., Bergvall et al. 2006; Izotov et al. 2016; Fletcher et al. 2019; Pérez-Montero et al. 2020). It turns these systems into perfect laboratories for the sutdy of LyC escape. Therefore, the discovery and characterization of local EELG analogs give us a way to gain more insight into the first moments of galaxy evolution when leakage of LyC photons from EELGs provided a major contribution to the EoR photon budget (e.g., Erb et al. 2016; Yang et al. 2017a; Naidu et al. 2022; Matthee et al. 2022).

Extreme-emission-line galaxies present spectra with very high EWs of [O III] and Hβ emission lines, and it has been found that these galaxies also used to be strong Lyα emitters (Tang et al. 2021). On the other hand, most typical LyC leakers presenting a very high EWs (Lyα) are frequently found among Green Pea galaxies, an outstanding family among the prototypes of EELGs (Izotov et al. 2016, 2018; Pérez-Montero et al. 2021).

As of today, observational studies have discovered thousands of EELGs, but most searches have produced a mixed bag of denominations, typically inspired by their compact optical appearance and/or color in plates; examples of these are Green Peas, Blue Berries, ELDots/HαDots, or SDSS extreme [H II] galaxies and their cohorts, to cite a few (e.g., Terlevich et al. 1991; Cardamone et al. 2009; Amorín et al. 2010, 2012; Bekki 2015; Yang et al. 2017b; Salzer et al. 2020), all illustrating how EELG selection can depend on the redshift range explored and the exact criteria and technique applied. The search for EELGs is somewhat complementary to the historical searches for blue galaxies of very compact morphology that were identified and analyzed in pioneering works since the middle of the last century (e.g., Haro 1956; Zwicky 1966; Markarian 1967). However, it is important to emphasize here that many of EELG searches performed so far have been based on broad-band photometry data, thus avoiding direct spectroscopic or narrow-band-based selection based on emission lines, which remain scarce (see, e.g., Indahl et al. 2021; Lumbreras-Calle et al. 2022; Iglesias-Páramo et al. 2022). This situation may have somehow supported the persistence of systematics and/or obvious bias in current samples

of EELG, given the typical very faint continua and the strong emission lines of these galaxies[1]. A clear example are the differences in the number and occurrence of these objects. Paalvast et al. (2018) explored galaxies with extreme [O III]/[O II] ratios, combining data from several MUSE Guaranteed Time Observing (GTO) programs ($0.28 < z < 0.85$) and founding 15 of these systems in their sample (3.7% of their total sample). Cardamone et al. (2009), imposing conditions on r_{SDSS}, redshift, optical colours, and morphology, reported a spatial density of Green Peas of approximately two per square degree, a critical benchmark in EELG studies. In the local Universe, Yang et al. (2017a) found a density of 0.003 EELGs per square degree for "blueberries" in the local Universe ($z \leq 0.05$), while Lumbreras-Calle et al. (2022) identified 466 EELGs within 2000 square degrees, equivalent to a density of about 0.23 per square degree, in the J-PLUS survey ($z \leq 0.06$). Furthermore, Amorín et al. (2015) reported 165 EELGs in the 1.7 square degree area covered by the zCOSMOS-bright survey, indicating a density of approximately 97 per square degree in the $0.11 \leq z \leq 0.93$ redshift range. As Iglesias-Páramo et al. (2022) noted, precise comparisons among different works are prevented by the different selection criteria and observational limits of each sample.

There is not a clear limit for the rest-frame equivalent width (EWo) to define a galaxy as an EELG. In this work, we used a similar definition for EELGs to that used by Iglesias-Páramo et al. (2022), that is, objects that show at least one emission line ([O II]$\lambda\lambda$3726, 3729, [O III]$\lambda\lambda$4959, 5007 or Hα) with EWo $\geq$300 Å. Nevertheless, we are aware that previous works have assumed different selection limits for EELGs (e.g., Amorín et al. 2015; Salzer et al. 2020; Iglesias-Páramo et al. 2022 and references therein); therefore, for the sake of consistency with previous works we enlarged our search producing an extended sample including all sources presenting EWo $\geq$200 Å. In this way, we gain consistency in order to compare with literature work, and we were able to examine the behavior of the main properties of EELGs around the adopted EWo limit; this an especially relevant exercise when looking for any possible evolution through redshift.

In this work, we took advantage of the exceptional depth and quality of the recent MUSE *Hubble* Ultra-Deep Field Survey data release (HUDFS; Bacon et al. 2023) to carry out a purely spectroscopic search for EELG with MUSE. EELGs usually show a compact appearance, although some low-surface-brightness structure can be seen for some of them (see Appendix A of Iglesias-Páramo et al. 2022 for examples). Here, we were able to spatially resolve the ionization structure and the gaseous kinematics of this type of object. This paper is organized as follows. In the next section, we summarize the observations and criteria to select the sample. Section 3 shows the basic properties of our EELG candidates. The results and discussion are presented in Sect. 4. The main conclusions are summarized in Sect. 5.

2. Data and sample

2.1. MUSE Hubble Ultra-Deep Field

The MUSE instrument is a powerful tool for optical (4750–9350 Å) spectroscopic studies thanks to a combination of a wide field of view (FoV) of $1' \times 1'$ with a spatial sampling of $0.2'' \times 0.2''$ per spaxel and high resolving power (ranging from 4R4 ~ 1800 in the blue to $R \sim 4000$ Å in the red). Our study is based in the second data release (DR2) of the *MUSE Hubble* Ultra-Deep Field Surveys (Bacon et al. 2023), which includes the deepest spectroscopic survey ever performed. With an achieved depth of 141 h and a field of view of 1 arcmin of diameter, it is a key addition to the previous MUSE spectroscopic survey data release (Bacon et al. 2017; Inami et al. 2017; DR1, a 3×3 arcmin^2 mosaic of nine MUSE fields at a 10-h depth and a single 1×1 arcmin^2 at 31-h depth) in the *Hubble* Ultra-Deep Field (Beckwith et al. 2006; HUDF) area. This second data release (DR2) incorporates the previous ones reprocessed with the same tools and methodology, providing a homogeneous data set of deep spectroscopic observations in the HUDF region.

In addition to the calibrated data, the data cubes have an extension with the propagated variance estimate, which is used in the line fitting process (see Sect. 3.1). Reduced and calibrated data cubes, the source catalogs, and an interactive browser are available to the public through the AMUSED web interface[2].

2.2. Sample selection

Our selection process begins by analyzing the information offered by the AMUSED interface. The main catalog gives a summary of source properties, and the final data cubes and associated images (e.g., *Hubble* images) are public for each object. We follow the criteria in Iglesias-Páramo et al. (2022) and define our primary sample of EELG as those objects that show at least one emission line with EWo $\geq$300 Å. We use the EWo measured by Bacon et al. (2023) using the python code pyPlatefit[3]. Briefly, pyPlatefit is an improved Python-based version of the PLATEFIT IDL software (Brinchmann et al. 2004) developed to fit MUSE data. It performs a stellar continuum fitting using a simple population model (Bruzual & Charlot 2003) and then fits the emission lines with Gaussian profiles after subtracting the continuum. To characterize the local continuum, `pyPlatefit` masks the emission lines and uses windows of 50 Å on the left and right.

Using these criteria, of the 2221 cataloged objects, we found a total of two, five, and three galaxies presenting rest-frame EWo $\geq$300 Å in [O II], [O III], and Hα, respectively. One of these objects presents EWo $\geq$300 Å in two lines ([O III] and Hα). Thus, we selected nine candidates (ID 91, 891, 895, 1795, 2478, 2532, 6465, 7373, and 7601) fulfilling the criteria for our primary EELG sample. A detailed closer inspection of the spectra of these nine candidates was performed on a one-by-one basis. In doing so, we found that the spectra of two of the candidates (ID 1795 and 7601) show low signal-to-noise ratios (SN) over the entire wavelength range, giving nonrealistic line fitting in the AMUSED database. Therefore, these two candidates were discarded from our EELG primary sample. Table 1 shows the basic properties of the sample; these include quantities extracted from AMUSED (MUSE ID, coordinates, redshift, magnitude in the HST *F775W* band, stellar mass, star formation rate, line of detection, line flux, corresponding luminosity,[4] and rest-frame EWo), and measurements of this work for line-flux and rest-frame EWo. All these relevant spectrophotometric properties are considered in the discussion.

[1] Pioneering spectroscopic surveys were carried out using wide field slitless spectroscopy techniques (see Salzer et al. 2000 and references there).

[2] https://amused.univ-lyon1.fr/

[3] https://pyplatefit.readthedocs.io/en/latest/tutorial.html

[4] We note that this luminosity is not corrected by the extinction of each galaxy. See Sect. 4.1.

Table 1. Basic properties of EELG primary sample candidates.

Muse ID	Ra (AMUSED) (deg)	Dec (AMUSED) (deg)	z (AMUSED)	mag_{F775W} (AMUSED)	log mass (AMUSED) $\log(\frac{M_{star}}{M_\odot})$	log SFR (AMUSED) $\log(\frac{M_\odot}{yr})$	Line	F (AMUSED) (10^{-20} erg s^{-1} cm^{-2})	log L (AMUSED) (erg s^{-1})	Cont (AMUSED) (10^{-20} erg s^{-1} cm^{-2} Å^{-1})	EWo (AMUSED) (Å)	F (this work) (10^{-20} erg s^{-1} cm^{-2})	Cont (this work) (10^{-20} erg s^{-1} cm^{-2} Å^{-1})	EWo (this work) (Å)
(1)	(2)	(3)	(4)	(5)	(6)	(7)	(8)	(9)	(10)	(11)	(12)	(13)	(14)	(15)
91	53.1625	–27.7803	0.72	26.18	8.26	–1.27	[O III]λ5007	4098	42.82	11.89	345	4099±6	11.89±0.45	345±13
891	53.1957	–27.7878	0.23	22.21	8.44	–0.54	Hα	67 946	44.04	218.37	311	67 942±15	218.37±0.46	311±1
895	53.1447	–27.7854	0.25	22.47	8.6	–0.64	[O III]λ5007	92 674	44.17	255.45	363	92 673±17	255.45±1.02	363±2
							Hα	57 498	43.96	173.54	331	57 500±9	173.54±0.46	331±1
2478	53.1839	–27.7954	0.73	27.85	7.19	–2.11	[O III]λ4959	583	41.97	1.55	375	583±3	1.55±0.26	375±98
							[O III]λ5007	2065	42.52	0.18	11 478$^{(\&)}$	2065±3	1.55±0.26	1332±224
2532	53.1497	–27.8093	0.75	27.91	7.44	–1.63	[O III]λ5007	492	41.9	1.27	387	492±5	1.27±0.37	386±97
6465	53.1942	–27.7854	0.72	26.15	–	–	[O III]λ5007	668	42.03	1.85	362	668±6	1.85±0.46	362±89
7373	53.1542	–27.7867	0.28	27.89	6.85	–2.43	Hα	102	41.21	0.33	307$^{(\&)}$	102±2	0.33±0.11	309±100

Notes. (1) MUSE source identifier; (2) right ascension (J2000.0); (3) declination (J2000.0); (4) redshift; (5) magnitude in HST $F775W$; (6) stellar mass; (7) star formation rate; (8) detected emission line with ≥300 Å; (9) flux of the emission feature; (10) luminosity of the emission feature; (11) flux of the continuum level; (12) rest-frame EW of the emission feature ($^{(\&)}$ uncertain value); (13) flux of the emission feature (measured in this work); (14) flux of the continuum level (measured in this work); (15) rest-frame EW of the emission feature (measured in this work).

Table 2. Same as Table 1, but for EELG extended sample candidates.

Muse ID	Ra (AMUSED) (deg)	Dec (AMUSED) (deg)	z (AMUSED)	mag_{F775W} (AMUSED)	log mass (AMUSED) $\log(\frac{M_{star}}{M_\odot})$	lo SFR (AMUSED) $\log(M_\odot\,yr^{-1})$	Line	F (AMUSED) (10^{-20} erg s^{-1} cm^{-2})	log L (AMUSED) (erg s^{-1})	Cont (AMUSED) (10^{-20} erg s^{-1} cm^{-2} Å^{-1})	EWo (AMUSED) (Å)	F (this work) (10^{-20} erg s^{-1} cm^{-2})	Cont (this work) (10^{-20} erg s^{-1} cm^{-2} Å^{-1})	EWo (this work) (Å)
(1)	(2)	(3)	(4)	(5)	(6)	(7)	(8)	(9)	(10)	(11)	(12)	(13)	(14)	(15)
1093	53.1763	–27.7809	0.54	24.87	7.92	–0.98	[O III]λ5007	5371	42.93	22.79	236	5364±9	22.79±0.38	235±4
1426	53.1473	–27.8008	0.28	26.05	7.07	–2.06	[O III]λ5007	2485	42.6	8.51	292	2485±5	8.51±0.29	292±10
1561	53.153	–27.7937	0.73	26.41	8.1	–1.3	[O III]λ5007	1450	42.37	5.72	254	1450±6	5.72 ±0.40	254±18
1699	53.154	–27.8052	0.67	26.70	7.93	–1.26	[O III]λ5007	905	42.16	3.98	228	905±5	3.98±0.24	228±14
6474	53.1866	–27.7902	0.12	23.20	–	–	[O III]λ5007	26 044	43.62	105.11	248	26 044±8	105.11±0.39	248±1
							Hα	15 343	43.39	73.78	208	15 343±7	73.78±0.48	208±1
6865	53.1604	–27.7752	0.83	26.60	–	–	[O III]λ5007	6276	43.00	25.73	244	6276±3	25.73±0.24	243±2

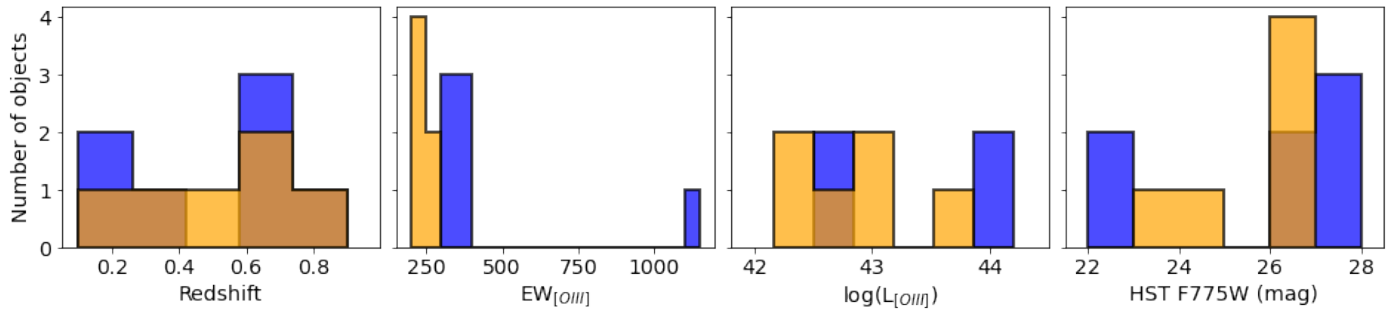

Fig. 1. Histograms of distribution of properties of EELG sample (see text for details).

Furthermore, as mentioned before, we also produced an extended EELG sample with sources presenting 200 Å ≤ EWo ≤ 300 Å in at least one of the lines considered above ([O II]$\lambda\lambda$3726, 3729, [O III]$\lambda\lambda$4959, 5007 or Hα). Using these extended criteria, we found a total of three, eight, and one galaxies showing 200 Å ≤ EWo ≤ 300 Å in [O II], [O III], and Hα, respectively. One of the objects detected in [O III] presents a EWo ≥300 Å in Hα (ID 7373) and one object shows 200 Å ≤ EWo ≤ 300 Å in both [O III] and Hα (ID 6474). Therefore, this gives ten candidates (ID 1093, 1426, 1561, 1699, 6474, 6865, 1863, 7105, 7985, 8000) for the extended EELG sample. We performed a detailed closer inspection of the spectra of these ten candidates, as was done for the primary sample. Following the same criteria, we end up discarding four galaxies (ID 1863, 7105, 7985 and 8000). The galaxies selected for our extended EELG sample are listed in Table 2.

Figure 1 shows the distribution of redshift, mag_{F775W}, $EWo_{[O\,III]}$[5] and $L_{[O\,III]}$. These candidates expand the following ranges: $0.1 < z < 0.9$, $22 < mag_{F775W} < 28$, 200 Å < EWo < 1200 Å and $41.9 \leq \mathrm{Log}(L_{[O\,III]}/\frac{erg}{s}) \leq 44.2$, respectively. We can see that both primary and extended samples share the same range of basic properties. We note that the low number of objects in our sample is totally expected based on reported densities of similar objects in the literature (e.g., Iglesias-Páramo et al. 2022). Furthermore, we do not find systems with a redshift ≤0.1 to be consistent with previous works based in the local Universe (e.g., Yang et al. 2017b; Lumbreras-Calle et al. 2022).

[5] We note that two galaxies (MUSE ID: 891 and 7373) are included in the primary sample performing its condition in $EWo_{H\alpha}$, though their $EWo_{[O\,III]}$ are lower than 300 Å.

3. Properties of the EELG sample

3.1. EELG spectra and line fluxes

Figure 2 shows the spectra of both EELG primary and extended samples. All the selected objects present characteristic spectra of strong-emission-line galaxies, consisting of a faint continuum and very prominent emission lines.

As we indicate in Sect. 2.2, our sample selection is based in the information given by the AMUSED web interface and

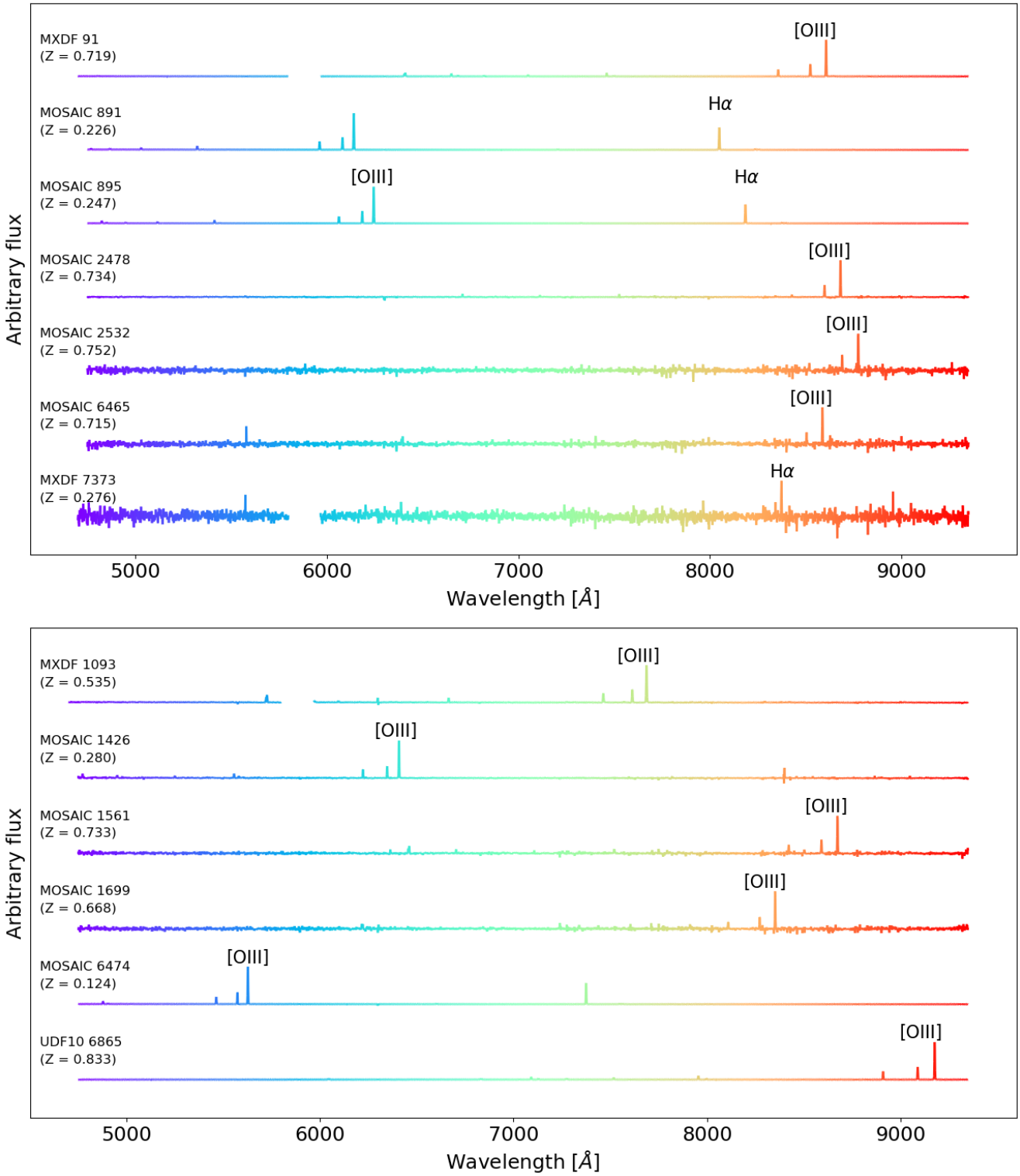

Fig. 2. Spectra for both our primary (top panel) and extended (bottom panel) EELG samples. MUSE ID, data set, redshift, and emission line used for the classification are indicated for each spectra.

the fittings performed by Bacon et al. (2023). The equivalent-width values depend on the continuum level, and this can be difficult to characterise. Therefore, we decide to re-evaluate the EWo values of our samples to confirm the EELG classification. Emission-line fitting was performed with `pyPlatefit`, including improvements with respect the previous fittings. Firstly, we use the parameter `ziter`, which allows a second iteration improving the fitting. Secondly, we perform 100 Monte Carlo simulations to compute uncertainties following standard procedures in full spectra-fitting techniques (e.g., del Moral-Castro et al. 2019, 2020; Bittner et al. 2019; Domínguez-Gómez et al. 2023, and references therein). Briefly, we derive these uncertainties creating multiple realisations of the original spectrum adding random noise consistent with the quality of the observed

spectrum to the best fit and running `pyPlatefit` again. The considered errors are the standard deviation of the 100 recovered values. Tables C.1 and D.1 present the fluxes measured for the emission lines for the primary and extended samples.

Thirdly, three objects (MUSE ID 91, 7373, and 1093) present a cut in the spectrum (from ∼5800 to ∼5970 Å). Then, to avoid possible problems with the fitting to the continuum, we fit the wavelength range from 6000 to 9300 Å. As for the rest of objects, the whole wavelength range was considered (4750–9300 Å). We notice that the object 2478 presents a very high EWo([O III]λ5007). This value seems to be too high, since the F([O III]λ4959) / ([O III]λ5007) is ∼1/3. Therefore, EWo([O III]λ5007) should be ∼3·EWo([O III]λ4959). However, it is ∼30. Through an inspection of the line catalog given by AMUSED, we found that the continuum associated with the [O III]λ5007 emission line is almost an order of magnitude lower than the continuum level of the [O III]λ4959 emission line. However, $F_{\rm cont}$([O III]λ4959)/$F_{\rm cont}$([O III]λ5007) ∼1 for the rest of the objects. Therefore, we decided to use the continuum level of the [O III]λ4959 emission line to compute the EWo([O III]λ5007) of MUSE ID 2478.

Finally, we studied the effect of the window width used by `pyPlatefit` to characterize the local continuum[6] on the EWo values. We used `pyPlatefit` to change the internal configuration to use windows of 100 and 200 Å confirming the EELG classification except for the object MUSE ID 7373, where the EWo values for windows of 100 and 200 Å are 102±11 and 106±7, respectively. Therefore, we added a flag of caution for this galaxy in Table 1.

3.2. Spectroscopic and spatially resolved properties

Figure 3 presents an example of photometric and spectroscopic properties derived for the galaxy ID 891. The upper row shows the HST 775W and MUSE white-light images, as well as the MUSE spectrum with an inset zoomed-in view around the Hγ and [O III]4363 Å emission lines. In the bottom row, we present the spatially resolved spectroscopic and kinematic information of the galaxy, which we discuss in Sect. 4.2. Emission-line fitting was performed using pyPlatefit spaxel by spaxel. The velocity field shows a clear pattern of rotation similar to those of nearby disk galaxies (i.e., Barrera-Ballesteros et al. 2014; del Moral-Castro et al. 2019). Only spaxels with significant line detections ($S/N > 6$) are shown. We checked that the results are not contingent upon the choice of the minimum S/N by repeating the analysis with different thresholds (3, 6, and 9). We prefer to maintain $S/N = 6$ to preserve the best possible spatial resolution for this analysis, combining it with a robust selection. Appendices A and B show similar images for the EELG primary and extended samples, respectively.

4. Results and discussion

4.1. Physical properties and chemical abundances

In order to compute the physical properties of the galaxies of our EELG sample,[7] we followed the expressions in Pérez-Montero (2017). The Balmer decrement was used for the derivation of the reddening coefficient C(Hβ) assuming the Case B approximation for electron temperature 15 000 K and density 100 cm^{-3} (Storey & Hummer 1995), and the extinction law by Cardelli et al. (1989) with $R_V = 3.1$. In any case, no relevant change is expected if the exact electron temperature and density of each object are used. Whenever possible, the ratio of the bright Balmer lines Hα/Hβ was used. When the flux measurement of Hα (ID 1426) or Hβ (ID 6465) is uncertain, or Hα is not observed (ID 2478). The C(Hβ) values for all the EELGs are presented in Table 3. After inspection of the errors of the flux of the Balmer lines considered above (see Appendices C and D), a formal 20% relative error (face value) was adopted for C(Hβ).

For two galaxies (ID 2478, ID 6465), the computed C(Hβ) was zero or slightly negative, though consistent to within the errors with the adopted value of C(Hβ) = 0. A C(Hβ) = 0 was adopted also for ID 2532 since only one Balmer line, Hβ, was measured for this galaxy. In what follows, all the fluxes used for the derivation of the physical properties and chemical abundances of the selected EELGs have been reddening-corrected accordingly.

Overall, the extinction values derived for our sample of EELGs are low, typically C(Hβ) ≈ 0.1 (Av ≈ 0.22), and the maximum is around Av ≈ 0.45, whereas a significant fraction of the sample shows values consistent with no extinction. This result, given the negligible Galactic extinction (Schlafly & Finkbeiner 2011), would translate into a low (or very modest) dust component associated with our EELGs, which is somewhat expected for low-metallicity (dwarf) galaxies.

For seven galaxies, the flux in the auroral [O III]λ4363 temperature-sensitive line was measured with a good signal-to-noise level, illustrating the high quality of the data. Therefore, we performed a direct calculation of their electron temperature, with significant implications for the chemical abundance derivation. We followed Pérez-Montero (2017) for the computation of the T[O III] electron temperature using the ([O III]λ5007

Table 3. Physical properties and chemical abundances.

ID	C(Hβ)	Te([O III]) (10^4 K)	Ne (cm^{-3})	log R_{23} (logO_3)	12+log(O/H)	Notes
91	0.11	1.65±0.04	≤50	0.89	7.72±0.03 [7.75]	(b) P
891	0.17	1.45±0.02	73	(0.76)	7.93±0.08	(a) P
895	0.18	1.38±0.01	75	(0.82)	7.99±0.08	(a) P
2478$^{(\star)}$	0.00	1.49±0.20	–	(0.95)	7.89±0.08	(a) P
2532$^{(\&)}$	0.00	–	–	(0.77)	–	(d) P
6465	0.00	–	90	1.03	7.77±0.10	(c) P
7373	0.22	–	–	(0.14)	–	(d) P
1093	0.09	1.31±0.12	≤ 50	0.81	7.90±0.10 [8.05]	(b) E
1426	0.20	–	≤50	0.75	7.47±0.10	(c) E
1561	0.13	–	≤50	0.83	7.58±0.10	(c) E
1699	0.10	–	544	0.77	7.51±0.10	(c) E
6474	0.13	1.69±0.06	496	(0.83)	7.72±0.08	(a) E
6865	0.12	2.08±0.05	557	0.76	7.38±0.02 [7.37]	(b) E

Notes. $^{(\star)}$ Hβ flux measurement uncertain. $^{(\&)}$ Only Hβ line flux measured; C(Hβ) = 0 assumed. Col. 7: (a) Oxygen abundance derived from Te([O III]) following the Amorín et al. (2015) relation; expected ±0.08 dex statistical error; (b) Oxygen abundance from the direct method; the abundance derived using (a) is also given in square brackets for comparison; (c) Oxygen abundance from R_{23} empirical calibration (Izotov et al. 2019; Williams et al. 2023); expected ±0.10 dex statistical error; (d) No oxygen abundance derived; only [O III] nebular line measured. P: primary EELG sample; E: extended EELG sample.

[6] Although, the broad-band *Hubble* Space Telescope (HST) observations are deeper than those of MUSE, the filter widths ($F606W$: 4632.15–7179.43 Å and $F775W$: 6801.41–8630.74 Å; see Fig. 1 of Bacon et al. 2023) are too large to ignore the presence of nonuniform spectral-energy-distribution (SED) components and other emission features in the characterization of the local continuum.

[7] A closer inspection of all individual line profiles confirmed the presence of narrow lines in all the sources, discarding AGN contamination. Furthermore, the BPT diagram was created for three of them, locating the galaxies in the star formation region.

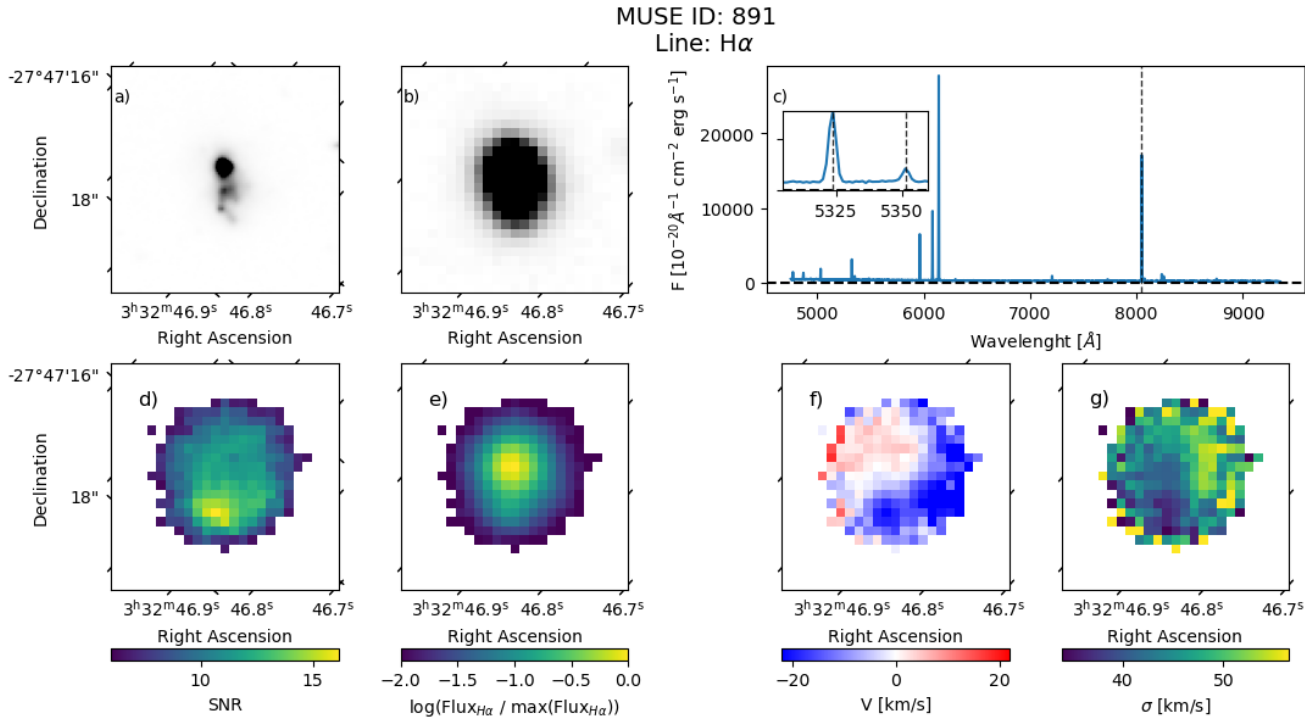

Fig. 3. MUSE ID 891: (a) HST *F775W* image with the spatial coverage of the MUSE data cube; (b) MUSE white light image of the galaxy; (c) spectrum of the object with an inset window showing a zoomed-in view around the Hγ and [O III]λ4363 emission lines; and maps of (d) S/N, (e) normalized flux, (f) relative radial velocity, and (g) velocity dispersion (σ), for the emission line indicated in the figure header.

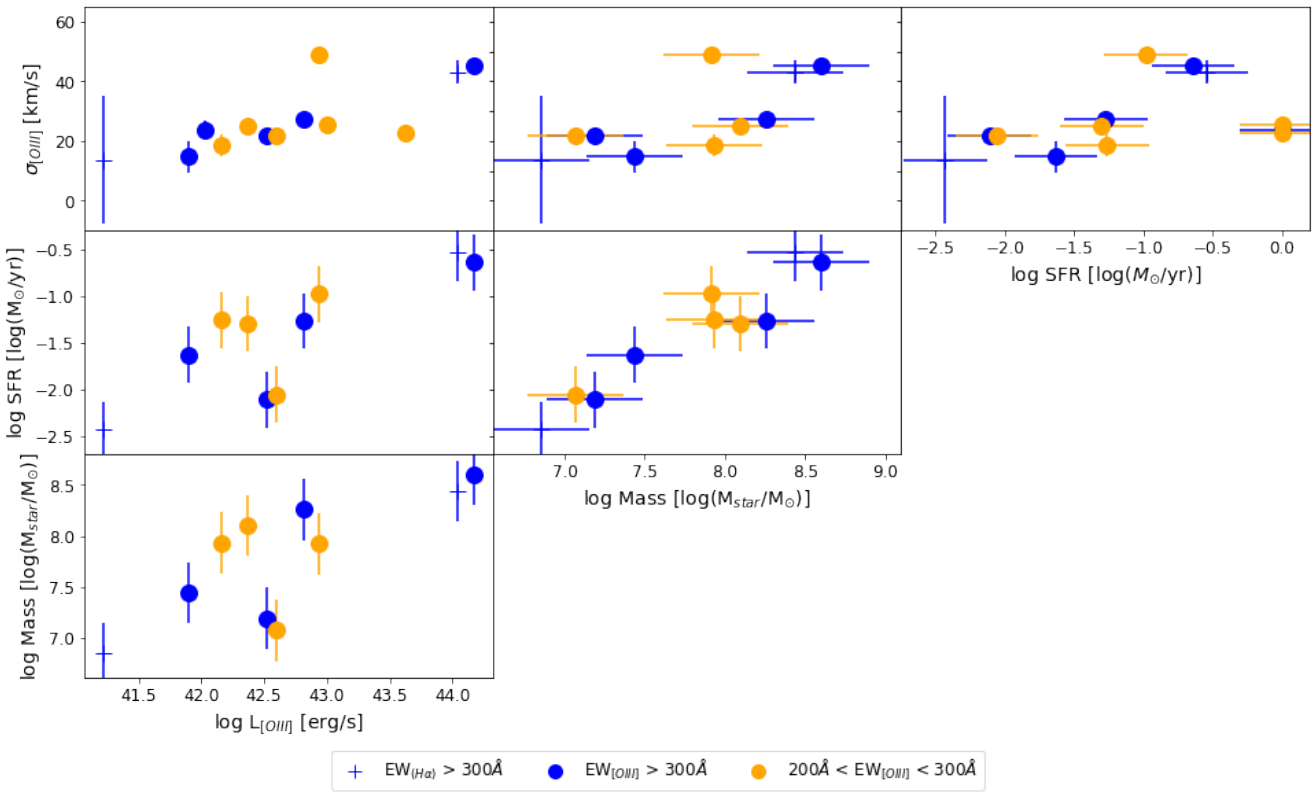

Fig. 4. Correlations between luminosity, stellar mass, star formation rate, and $\sigma_{[\mathrm{O\,III}]}$. We assume typical uncertainties of 0.3dex for mass and star formation rate (see Bacon et al. 2023).

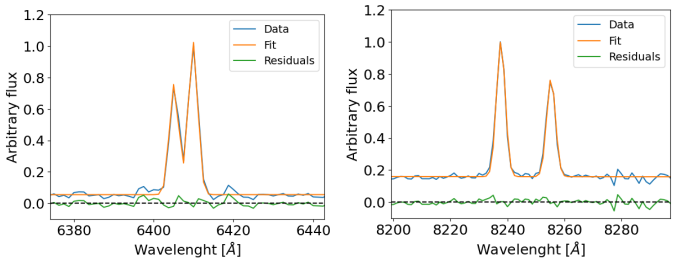

Fig. 5. Electron density sensitive lines. *Left panel*: fit to [O II]$\lambda\lambda$3726, 3729 doublet in spectrum of galaxy ID 91. *Right panel*: fit to [S II]$\lambda\lambda$6717, 6731 doublet in spectrum of galaxy ID 891. In each plot, the observed spectrum (blue), its fit (orange), and the residuals (green) are shown.

+[O III]λ4959)/[O III]λ4363 line ratio. The values of T[O III] obtained, along with their corresponding errors derived via error propagation from the measured flux error, are presented in Table 3. The T[O III] electron temperatures are high, ranging from 1.3×10^4 K to over 20×10^4 K; these temperature values are typically found in low-metallicity star-forming galaxies (e.g., Amorín et al. 2015; Kehrig et al. 2016; Izotov et al. 2019; Pérez-Montero et al. 2021).

The electron density, N_e, was derived using the line ratios from the [O II]$\lambda\lambda$3726, 3729 and [S II]$\lambda\lambda$6717, 6731 doublets whenever observed (redshift permitting; see Fig. 5 for an example), with both line doublets being resolved in the MUSE data. For galaxies ID 91, 6465, 1093, 1426, 1561, 1699, 6865, we have measurements of the [O II]$\lambda\lambda$3726, 3729 doublet, whereas the [S II]$\lambda\lambda$6717, 6731 doublet is measured for ID 891, 895, 6474. For three galaxies, ID 2478, 2532, 7373, we have no information to derive the electron density. We assume an electron temperature of 10^4 K (Sanders et al. 2016; Harshan et al. 2020). After a close inspection of the measured flux errors, in this work we adopted a formal relative error for N_e of 20% (face value) and a value of the low density limit for $N_e \leq 50$ cm^{-3}. The electron densities derived for our EELG galaxies are shown in Table 3. These values of electron density indicate that most galaxies of the sample have a low density, and N_e in four of them is consistent with the low-density limit. However, for three galaxies, IDs 1699, 6474, and 6865, substantially high electron densities are derived, with $N_e \approx 500$ to 600 cm^{-3}. Interestingly, two of them, ID 6474 and ID 6865, show the highest electron temperatures derived.

After obtaining the physical properties of the galaxies above, we derived their metallicity using the spectroscopic information gathered. We calculated the oxygen chemical abundance of the ionized gas of these EELGs, as a direct measurement of their gas metallicity. To do so, we proceeded as follows.

1. For galaxies (ID 91, 1093[8], 6865) for which we have measurements of the [O II]$\lambda\lambda$3726, 3729 and [O III]$\lambda\lambda$5007, 4959 flux, together with the electron temperature T[O III], we can perform a direct derivation of the ionic O^+/H^+ and O^{++}/H^+ abundances, adding them up to derive the total oxygen abundance, expressed as 12+log(O/H). For this calculation, a two-ionization-zone scheme was adopted following Pérez-Montero (2017), using T[O III] for the O^{++} zone and estimating the O^+ zone temperature T[O II]. The 12+log(O/H) of these galaxies, along with their corresponding errors estimated from error propagation of line fluxes and temperature, are quoted in Table 3.

[8] A second fitting in the rest-frame 4000–5800 Å was perfomed to fit the [O II]$\lambda\lambda$3726, 3729 doublet.

2. For galaxies (ID 891, 895, 2478, 6474) for which we derived the electron temperature, T[O III], but no [O II]$\lambda\lambda$3726, 3729 lines are measured, we cannot proceed with the direct method as above. In these cases, we rely on the anticorrelation between the total oxygen abundance of the ionized gas and its electron temperature, as observed in Amorín et al. (2015); this is a direct, theoretically expected consequence of the cooling of the ionized gas via oxygen lines. The values of 12+log(O/H) for these galaxies, along with the corresponding statistical error ±0.08 dex, were derived following the expression in Amorín et al. (2015) and are presented in Table 3. For the sake of comparison, we derived 12+log(O/H) also for the three galaxies treated with the direct method above, giving a very good agreement within the errors.

3. For the rest of the galaxies, we only have flux measurements of the [O II]$\lambda\lambda$3726, 3729 and [O III]$\lambda\lambda$5007, 4959 lines, for ID 6465, 1426, 1561, 1699, or even only [O III]$\lambda\lambda$5007, 4959 for ID 2532, 7373. In this third case, in order to determine the oxygen abundance we have to rely on an empirical calibration of abundance based on bright lines. Among the empirical calibrations, the one based on the R_{23} parameter, originally defined by Pagel et al. (1979) as R_{23} = ([O II]$\lambda\lambda$3726, 3729 +[O III]$\lambda\lambda$5007, 4959)/Hβ, stands out as a useful and robust tool against possible ionization structure effects (e.g., Relaño et al. 2010; Kehrig et al. 2016). In this work, we made use of the R_{23} calibration (Izotov et al. 2019) to derive the oxygen abundance 12+log(O/H). However, the R_{23} calibration is bi-valuated, and additional information is required to choose the appropriate branch; thus, we applied it as in Williams et al. (2023), selecting the low-metallicity regime taking into account the high [O III]$\lambda\lambda$5007, 4959/[O II]$\lambda\lambda$3726, 3729 measured for the EELG galaxies (e.g., Sanders et al. 2016). The derived 12+log(O/H) abundances and their corresponding statistical errors of ±0.1 dex are presented in Table 3. We also show the values of R_{23} when available, or $\log O_3$=[O III]$\lambda\lambda$5007, 4959)/Hβ when [O II]$\lambda\lambda$3726, 3729 lines are not measured.

It has been reported that the ionized interstellar medium in some extreme-emission-line galaxies could be experiencing density-bounded conditions (e.g., Jaskot & Oey 2013). These objects would show extreme [O III]$\lambda\lambda$5007, 4959/[O II]$\lambda\lambda$3737, 3729 flux ratios (typically $\gtrsim$40), suggestive of the presence of nonstandard conditions, which may complicate the applicability of abundance calibrations. The abundance calibration applied in this work is selected from Izotov et al. (2019), and it was specifically derived for the class of extreme emission line low-metallicity galaxies studied here. All sample galaxies for which the empirical calibration has been applied present moderate to low values of the [O III]$\lambda\lambda$5007, 4959/[O II]$\lambda\lambda$3737, 3729 ratio (see Tables C.1, D.1); hence, any potential effect associated with density bounded conditions is expected to be minor. The analysis of the oxygen abundances derived for our EELG sample indicates that these galaxies are all metal poor, with $7.35 \leq 12 + \log(O/H) \leq 8.05$, with four of them showing a metallicity below 0.1 solar. The very low metallicities obtained in our search for EELGs have significant implications for their characterization as local analogs of the earliest star-forming galaxies.

4.2. Kinematical properties, structure, and velocity maps

By inspecting the kinematics maps presented in Sect. 3.2, we can separate our sample in three different classes. These are listed below.

1. Resolved with kinematic pattern[9]: Spatially resolved galaxies that show a clear pattern of rotation (i.e., presence of a disk, with the velocity increasing outward). ∼43% of EELGs in the primary sample are in this class. They include the following: (i) ID 891: The HST *F775W* continuum image reflects a nonnuclear shape, with several high-surface-brightness knots connected by a diffuse low-surface-brightness component. This structure is not shown in the MUSE white light image (given the lower spatial resolution), which presents a head-tail shape (i.e., a main, bright, star-forming clump located at the center of the image and a low-surface-brightness tail). The S/N map shows its highest values in the inner galaxy, though these peak slightly south of the flux maximum, which is likely a consequence of the different line profile shapes and the higher velocity dispersion measured. The ionized-gas-velocity field presents a clear rotating disk structure, showing higher values in the region corresponding to the knots identified in the HST image. We note that these knots could be reminiscent of the structures seen in tidal dwarf and/or cometary galaxies (e.g., Lagos et al. 2016; Roche et al. 2023). These galaxies are usually considered the result of a tidal process or interactions of disk galaxies. No apparent companion is envisaged in this figure; however, further investigation on its true nature is beyond the scope of this paper; (ii) ID 895: The HST image shows an elongated shape, which is also reflected by the MUSE white light image. The [O III] S/N map shows a nuclear shape, while the Hα map also presents an elongated shape, with the highest values peaking slightly south of the flux maximum. Both [O III] and Hα flux maps present a nuclear shape peaking at the center of the galaxy. The [O III] and Hα velocity field show clear rotation disk structures; (iii) ID 91: The HST *F775W* image presents a nuclear shape. This shape is also shown in the MUSE white-light, S/N, and flux maps. The [O III] velocity field shows a rotating pattern.

2. Resolved without kinematic pattern: These are spatially resolved galaxies, but, unlike the previous category, they do not show a rotation pattern. This class represents ∼14% and ∼83% of our EELGs (ID: 2478) and extended samples, respectively (ID: 1093, 1426, 1561, 6474, and 6865). The HST *F775W* images reflect a nuclear shape, except for the ID 6474 object, which presents an elongated shape with a low-surface-brightness tail. The nuclear shape is also presented in the MUSE white light, S/N, and flux maps for the six galaxies.

3. Not resolved: These are galaxies whose structure cannot be resolved. ∼43% and ∼17% of both, EELGs primary (ID: 2532, 6465 and 7373) and extended (ID: 1699) samples, respectively, are included in this class.

We note that we applied a similar approach to Guérou et al. (2017), considering a galaxy spatially resolved if the galaxy has an area of at least 16 MUSE spaxels (i.e., about 1.5 times the PSF FWHM size of the data cube). We are aware that mergers may mimic the appearance of rotation patterns in observations of finite spatial resolution. Therefore, observations with better spatial resolution (e.g., JWST or MUSE-NFM observations) are necessary to reliably determine the internal structure of these systems.

4.3. Global properties and evolution

Figure 4 displays the relations among the derived [O III] luminosity and velocity dispersion, stellar mass and SFR (both parameters taken from the AMUSED database, as derived using the Prospector code[10]), for both the primary and extended samples. Inspection of this figure first reveals that, when comparing the behavior of both samples, no clear differences can be found between them, i.e. the EWo limits assumed to select our EELGs do not seem to introduce a bias in their observed properties. Overall, all four parameters show good correlations, with the SFR versus stellar mass plot delineating a very clear main sequence for our sample of EELGs. From the ionized gas, the derived [O III] line luminosity and σ correlate, both parameters showing some degree of correlation versus stellar mass and SFR, most notably between stellar mass and [O III] luminosity. This is relevant since we are comparing properties, e.g. [O III] luminosity and stellar mass, which were independently derived, corresponding to gaseous and stellar components of the EELG galaxies, respectively.

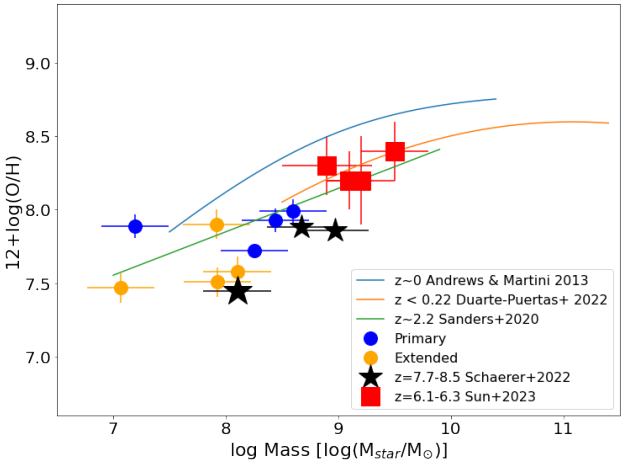

Fig. 6. Mass-metallicity relation. Oxygen chemical abundance and stellar mass for galaxies in the primary (blue circles) and extended (orange circles) samples in this work, compared to mean relations observed at z∼0 (Andrews & Martini 2013), z<0.22 (Duarte Puertas et al. 2022), and z = 2.2 (Sanders et al. 2016). Black stars and red squares show recent results for high-redshift galaxies from JWST data (Schaerer et al. 2022; Sun et al. 2023).

In Fig. 6, we present the mass-metallicity relation showing average loci corresponding to nearby (SDSS) and high-redshift galaxies. Our EELG galaxies[11], sampling the low-stellar-mass (mass$_{pro}$ ≤9.0) and low-metallicity (12+log(O/H)≤8.0) regions of the plot, are consistent with the mass–metallicity relation derived for z∼2.2 (Sanders et al. 2016) galaxies. They are also close to the locus defined by very-high-redshift objects (z = 7.7–8–5 and z = 6.1–6.3), as recently studied by Schaerer et al. (2022) and Sun et al. (2023) using JWST data. This result illustrates how the EELGs in our sample can be considered true local analogs of these high-redshift systems. The next generation of ground-based 30-m telescopes, together with additional observations from space, will allow us to fill this figure with low metallicity and low massive EELG galaxies at high-redshift and their local analogs.

5. Summary

For decades, EELGs searches have been performed on broad-band photometry data. Recently, thanks to the development of

[9] We note that this class presents significantly larger velocity amplitudes.

[10] All the details of the derivation of stellar mass and SFR can be found in Bacon et al. (2023).

[11] Only eight of the galaxies in Table 3 have stellar mass values in the AMUSED database.

new instruments and recent surveys such as SDSS or J-PAS, direct spectroscopy or narrow-band searches have been carried out (e.g., Indahl et al. 2021; Iglesias-Páramo et al. 2022). However, the number of EELG searches and analyses performed to date based on IFU data is (to our knowledge) very scarce. In fact, this work could be considered among the first EELG searches performed based on deep IFU data surveys, since previous works have mostly studied specific objects (e.g., Lofthouse et al. 2017; Bosch et al. 2019; Arroyo-Polonio et al. 2023).

Taking advantage of the deepest IFU survey to date, we present spatially resolved kinematic maps for a sample of intermediate redshift EELGs observed from the ground. Furthermore, we confirm that these systems are true local analogs of high-redshift systems (z = 6–8) studied by the JWST. While these cases already reveal the fantastic potential of the MUSE Ultra Deep Field data set, our small sample prevents a more detailed study of the basic properties of EELGs. However, this work can be regarded as a successful pilot study, demonstrating the power of the presented methodology to analyze strong emission-line galaxies using IFU data. Future deep observations with MUSE or ongoing instruments such as HARMONI will result in a larger sample to which to apply the methodology presented here.

Acknowledgements. We thank the referee for carefully reading our manuscript and providing constructive comments improving the paper. This study uses data provided by the Muse *Hubble* Ultra Deep survey, publicly available at the AMUSED database (`https://amused.univ-lyon1.fr/`). I.M.C. acknowledges funding from U. La Laguna through the Margarita Salas Fellowship from the Spanish Ministry of Universities ref. UNI/551/2021-May 26 and under the EU Next Generation funds, and from ANID programme FONDECYT Postdoctorado 3230653. J.M.V., J.I.P., A.A.P. acknowledge financial support from grants CEX2021-001131-S and PID2019-107408GB-C44 funded by MCIN/AEI/ 10.13039/501100011033. This paper makes use of python (`http://www.python.org`); Matplotlib (Hunter 2007): a suite of open-source python modules that provide a framework for creating scientific plots; Astropy (`http://www.astropy.org`): a community-developed core Python package and an ecosystem of tools and resources for astronomy (Astropy Collaboration et al. 2013, 2018, 2022); MPDAF (`https://mpdaf.readthedocs.io`): an open-source Python package that provides tools to work with MUSE-specific data; and pyplatefit (`https://github.com/musevlt/pyplatefit`) (Bacon et al. 2023): a python routine for emission and absorption lines fit of MUSE spectra. and AMUSED (`https://amused.univ-lyon1.fr/`): a public web interface for inspection and retrieval of extragalactic MUSE data products. IMC thank Alejandro S. Borlaff for helpful discussions on the HST broad-band images.

References

Amorín, R. O., Pérez-Montero, E., & Vílchez, J. M. 2010, ApJ, 715, L128
Amorín, R., Vílchez, J. M., Hägele, G. F., et al. 2012, ApJ, 754, L22
Amorín, R., Pérez-Montero, E., Contini, T., et al. 2015, A&A, 578, A105
Andrews, B. H., & Martini, P. 2013, ApJ, 765, 140
Arroyo-Polonio, A., Iglesias-Páramo, J., Kehrig, C., et al. 2023, A&A, 677, A114
Astropy Collaboration (Robitaille, T. P., et al.) 2013, A&A, 558, A33
Astropy Collaboration (Price-Whelan, A. M., et al.) 2018, AJ, 156, 123
Astropy Collaboration (Price-Whelan, A. M., et al.) 2022, ApJ, 935, 167
Bacon, R., Conseil, S., Mary, D., et al. 2017, A&A, 608, A1
Bacon, R., Brinchmann, J., Conseil, S., et al. 2023, A&A, 670, A4
Barrera-Ballesteros, J. K., Falcón-Barroso, J., García-Lorenzo, B., et al. 2014, A&A, 568, A70
Beckwith, S. V. W., Stiavelli, M., Koekemoer, A. M., et al. 2006, AJ, 132, 1729
Bekki, K. 2015, MNRAS, 454, L41
Bergvall, N., Zackrisson, E., Andersson, B. G., et al. 2006, A&A, 448, 513
Bittner, A., Falcón-Barroso, J., Nedelchev, B., et al. 2019, A&A, 628, A117
Bosch, G., Hägele, G. F., Amorín, R., et al. 2019, MNRAS, 489, 1787
Brinchmann, J., Charlot, S., White, S. D. M., et al. 2004, MNRAS, 351, 1151
Bruzual, G., & Charlot, S. 2003, MNRAS, 344, 1000
Cardamone, C., Schawinski, K., Sarzi, M., et al. 2009, MNRAS, 399, 1191
Cardelli, J. A., Clayton, G. C., & Mathis, J. S. 1989, ApJ, 345, 245
Dayal, P., & Ferrara, A. 2018, Phys. Rep., 780, 1
del Moral-Castro, I., García-Lorenzo, B., Ramos Almeida, C., et al. 2019, MNRAS, 485, 3794
del Moral-Castro, I., García-Lorenzo, B., Ramos Almeida, C., et al. 2020, A&A, 639, A9
Domínguez-Gómez, J., Pérez, I., Ruiz-Lara, T., et al. 2023, Nature, 619, 269
Duarte Puertas, S., Vilchez, J. M., Iglesias-Páramo, J., et al. 2022, A&A, 666, A186
Erb, D. K., Pettini, M., Steidel, C. C., et al. 2016, ApJ, 830, 52
Fletcher, T. J., Tang, M., Robertson, B. E., et al. 2019, ApJ, 878, 87
Guérou, A., Krajnović, D., Epinat, B., et al. 2017, A&A, 608, A5
Haro, G. 1956, Bol. Observatorios Tonantzintla Tacubaya, 2, 8
Harshan, A., Gupta, A., Tran, K.-V., et al. 2020, ApJ, 892, 77
Hunter, J. D. 2007, Comput. Sci. Eng., 9, 90
Iglesias-Páramo, J., Arroyo, A., Kehrig, C., et al. 2022, A&A, 665, A95
Inami, H., Bacon, R., Brinchmann, J., et al. 2017, A&A, 608, A2
Indahl, B., Zeimann, G., Hill, G. J., et al. 2021, ApJ, 916, 11
Izotov, Y. I., Schaerer, D., Thuan, T. X., et al. 2016, MNRAS, 461, 3683
Izotov, Y. I., Worseck, G., Schaerer, D., et al. 2018, MNRAS, 478, 4851
Izotov, Y. I., Guseva, N. G., Fricke, K. J., & Henkel, C. 2019, A&A, 623, A40
Jaskot, A. E., & Oey, M. S. 2013, ApJ, 766, 91
Kehrig, C., Vílchez, J. M., Pérez-Montero, E., et al. 2016, MNRAS, 459, 2992
Lagos, P., Demarco, R., Papaderos, P., et al. 2016, MNRAS, 456, 1549
Lofthouse, E. K., Houghton, R. C. W., & Kaviraj, S. 2017, MNRAS, 471, 2311
Lumbreras-Calle, A., López-Sanjuan, C., Sobral, D., et al. 2022, A&A, 668, A60
Markarian, B. E. 1967, Astrofizika, 3, 24
Matthee, J., Naidu, R. P., Pezzulli, G., et al. 2022, MNRAS, 512, 5960
Naidu, R. P., Matthee, J., Oesch, P. A., et al. 2022, MNRAS, 510, 4582
Paalvast, M., Verhamme, A., Straka, L. A., et al. 2018, A&A, 618, A40
Pagel, B. E. J., Edmunds, M. G., Blackwell, D. E., Chun, M. S., & Smith, G. 1979, MNRAS, 189, 95
Pérez-Montero, E. 2017, PASP, 129, 043001
Pérez-Montero, E., Kehrig, C., Vílchez, J. M., et al. 2020, A&A, 643, A80
Pérez-Montero, E., Amorín, R., Sánchez Almeida, J., et al. 2021, MNRAS, 504, 1237
Ravindranath, S., Monroe, T., Jaskot, A., Ferguson, H. C., & Tumlinson, J. 2020, ApJ, 896, 170
Relaño, M., Monreal-Ibero, A., Vílchez, J. M., & Kennicutt, R. C. 2010, MNRAS, 402, 1635
Roche, N., Vílchez, J. M., Iglesias-Páramo, J., et al. 2023, MNRAS, 523, 270
Salzer, J. J., Gronwall, C., Lipovetsky, V. A., et al. 2000, AJ, 120, 80
Salzer, J. J., Feddersen, J. R., Derloshon, K., et al. 2020, AJ, 160, 242
Sanders, R. L., Shapley, A. E., Kriek, M., et al. 2016, ApJ, 816, 23
Schaerer, D., Marques-Chaves, R., Barrufet, L., et al. 2022, A&A, 665, L4
Schlafly, E. F., & Finkbeiner, D. P. 2011, ApJ, 737, 103
Stark, D. P. 2016, ARA&A, 54, 761
Storey, P. J., & Hummer, D. G. 1995, MNRAS, 272, 41
Sun, F., Egami, E., Pirzkal, N., et al. 2023, ApJ, 953, 53
Tang, M., Stark, D. P., Chevallard, J., et al. 2021, MNRAS, 503, 4105
Terlevich, R., Melnick, J., Masegosa, J., Moles, M., & Copetti, M. V. F. 1991, A&AS, 91, 285
Williams, H., Kelly, P. L., Chen, W., et al. 2023, Science, 380, 416
Yang, H., Malhotra, S., Gronke, M., et al. 2017a, ApJ, 844, 171
Yang, H., Malhotra, S., Rhoads, J. E., & Wang, J. 2017b, ApJ, 847, 38
Zwicky, F. 1966, ApJ, 143, 192

Appendix A: Spectra and images of the primary EELG sample candidates

In this appendix, we show both the spectra and the images of the selected EELG candidates.

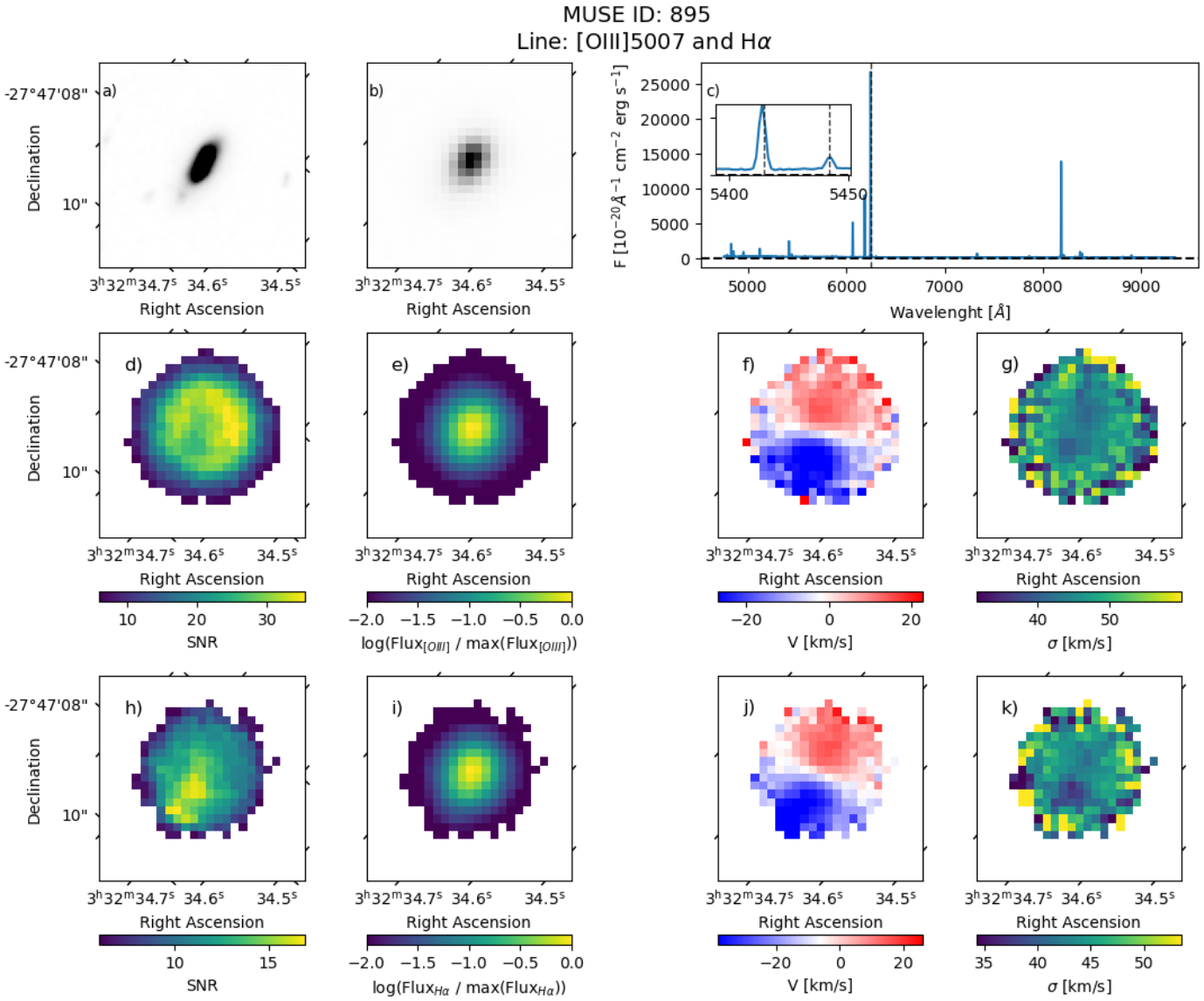

Fig. A.1. Same as Fig. 3, but for MUSE ID galaxy 895.

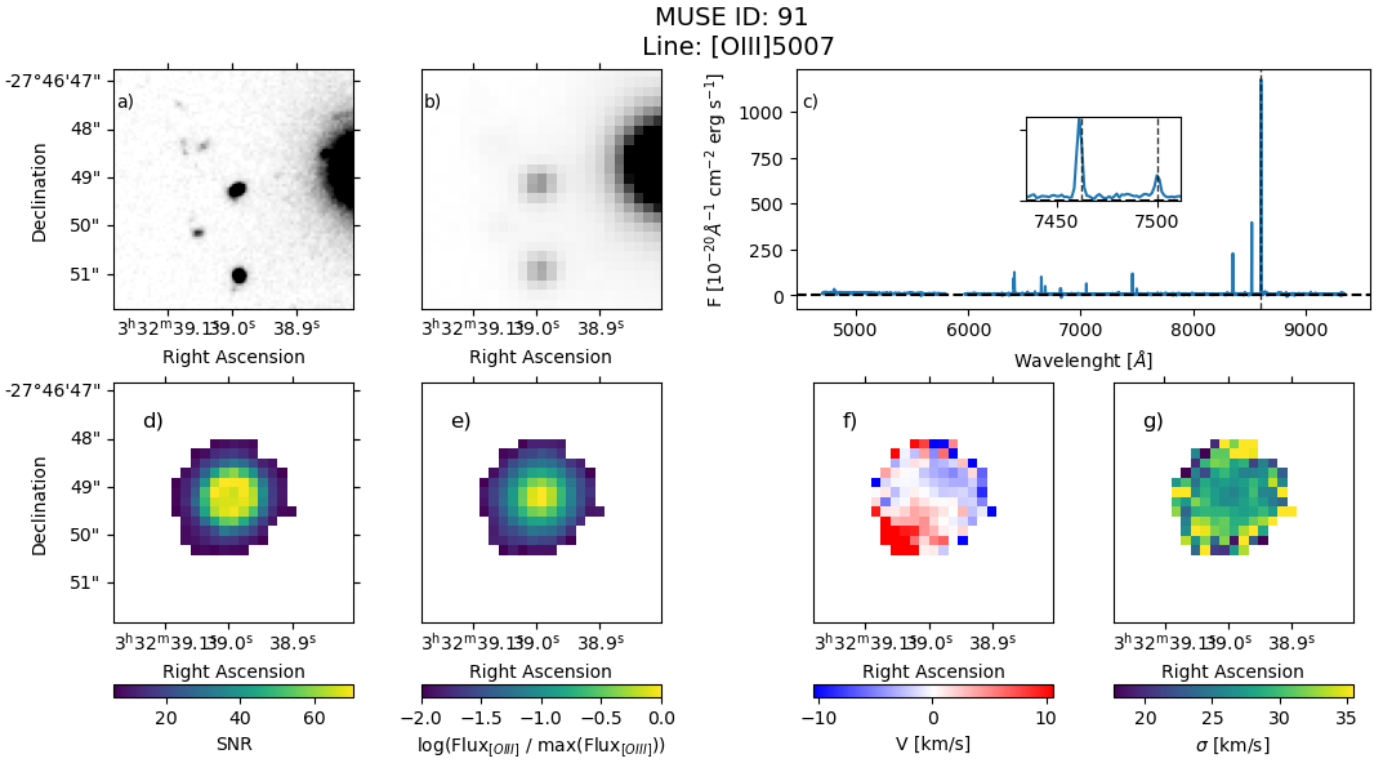

Fig. A.2. Same as Fig. 3, but for MUSE ID galaxy 91.

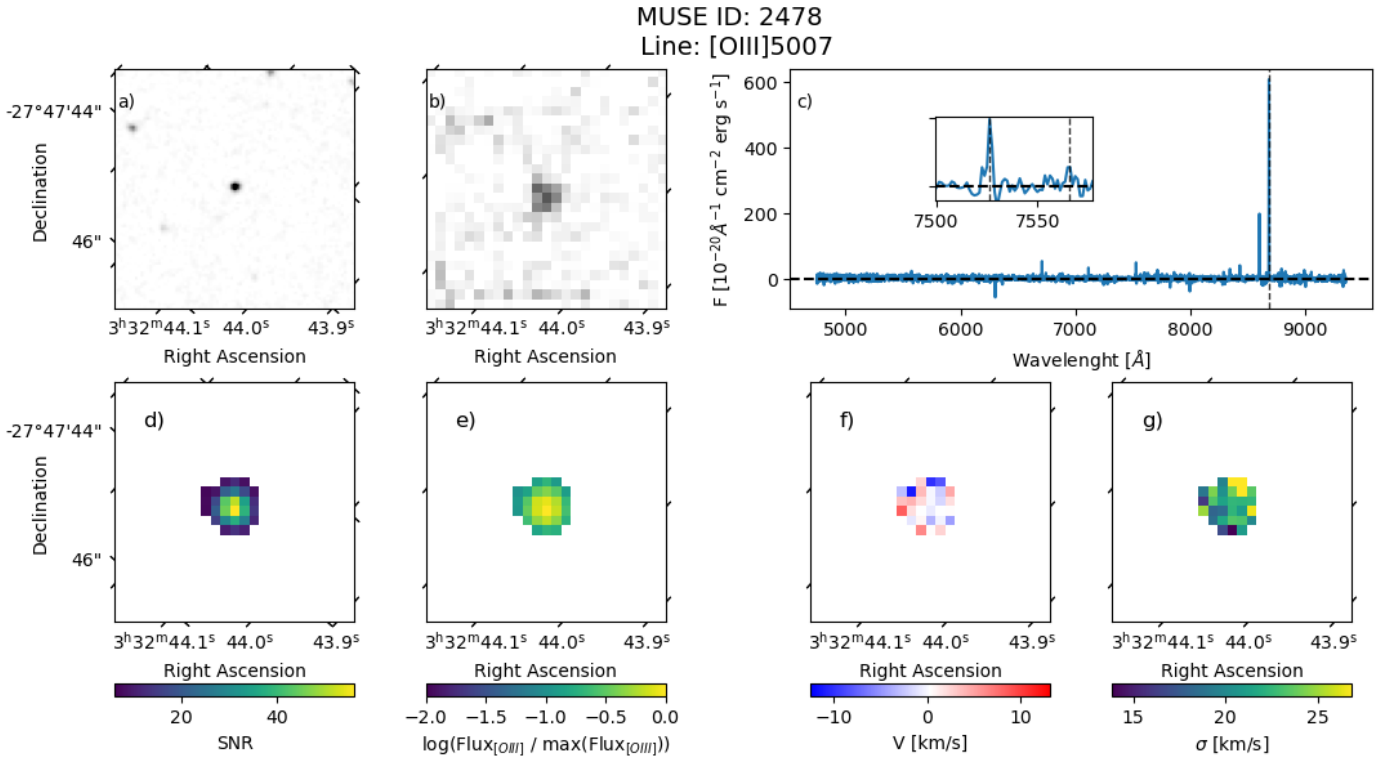

Fig. A.3. Same as Fig. 3, but for MUSE ID galaxy 2478.

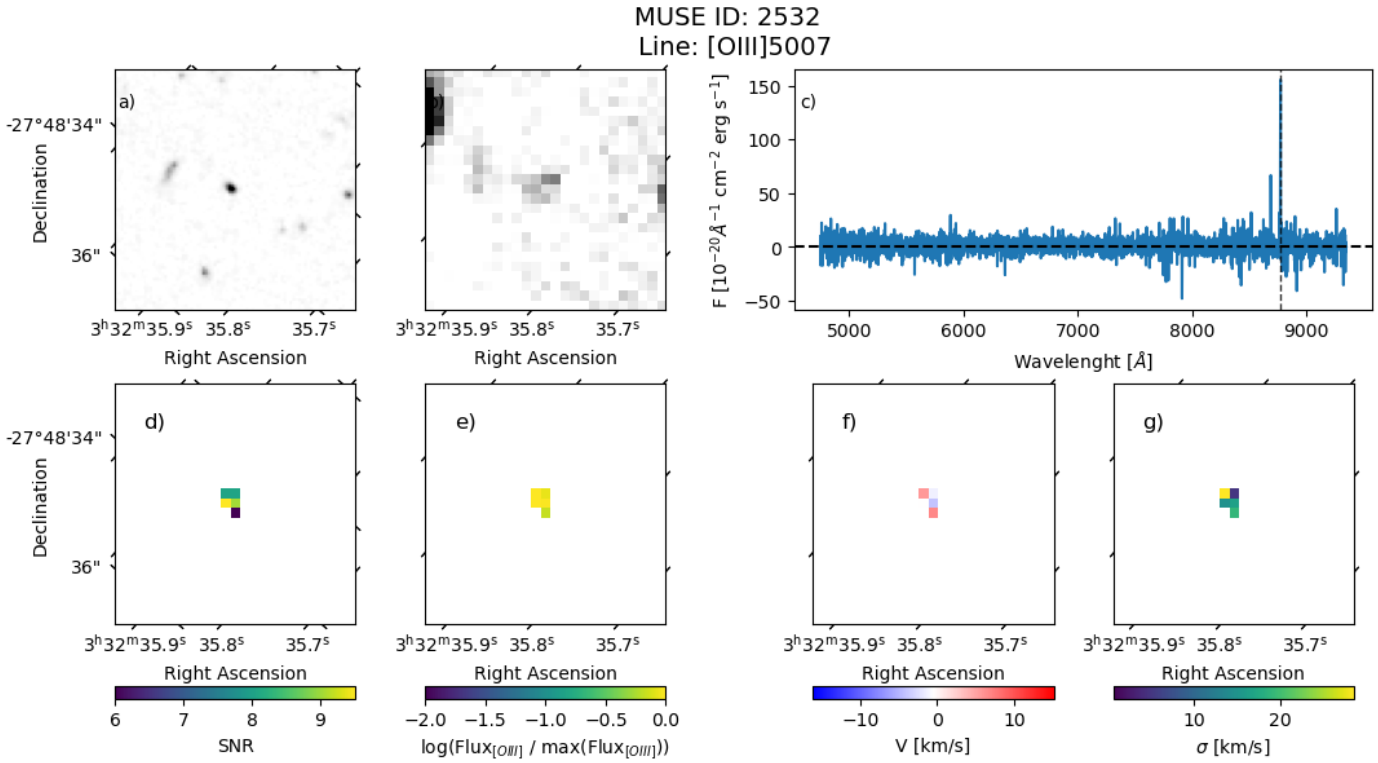

Fig. A.4. Same as Fig. 3, but for MUSE ID galaxy 2532.

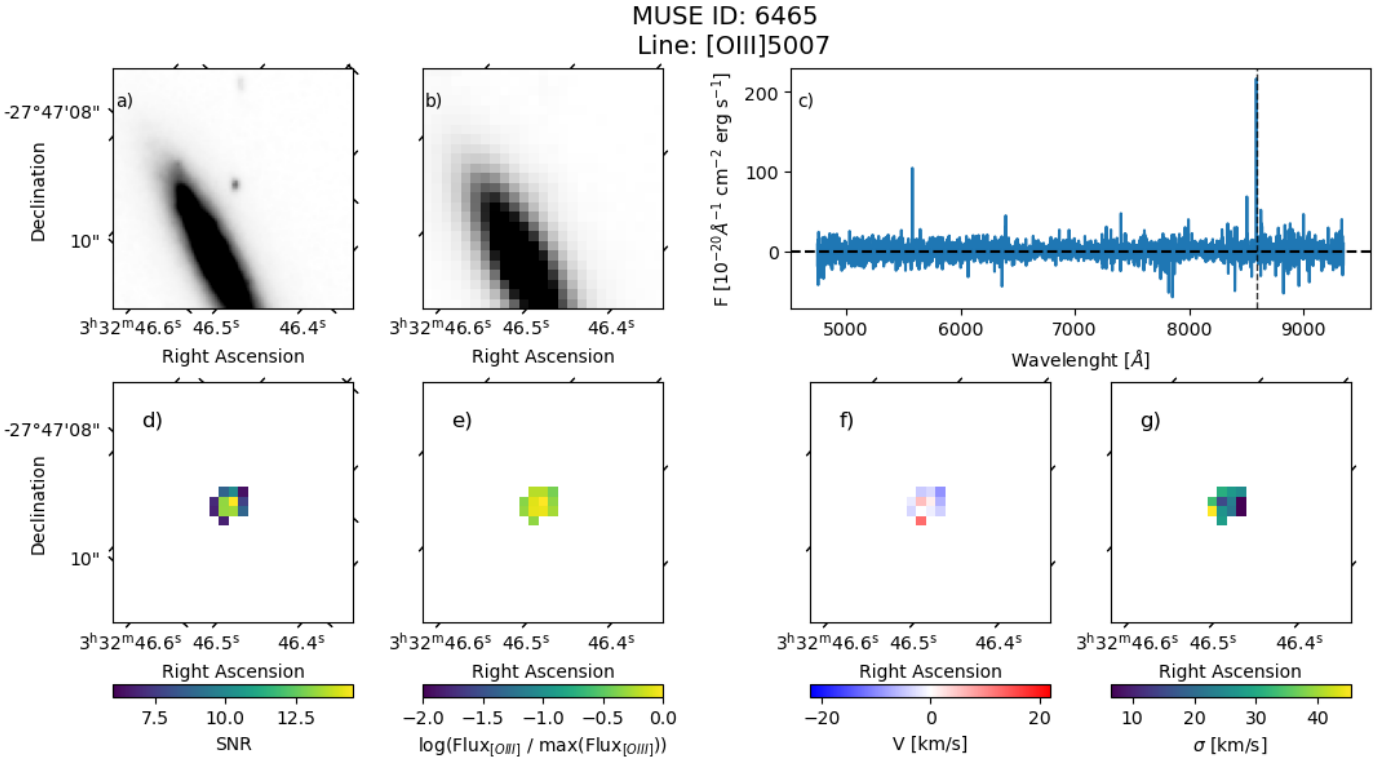

Fig. A.5. Same as Fig. 3, but for MUSE ID galaxy 6465.

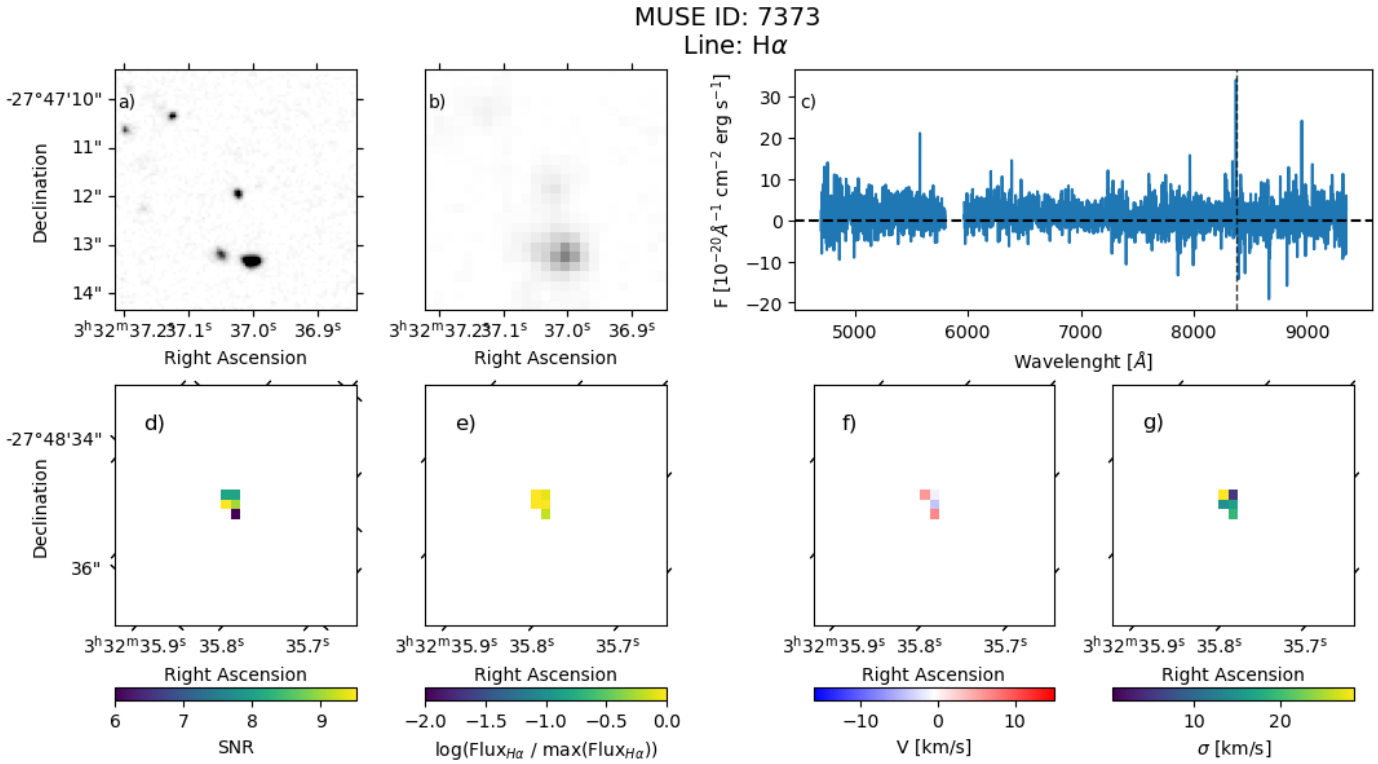

Fig. A.6. Same as Fig. 3, but for MUSE ID galaxy 7373.

Appendix B: Spectra and images of the EELG extended sample

Here, we present both the spectra and the images of the extended sample.

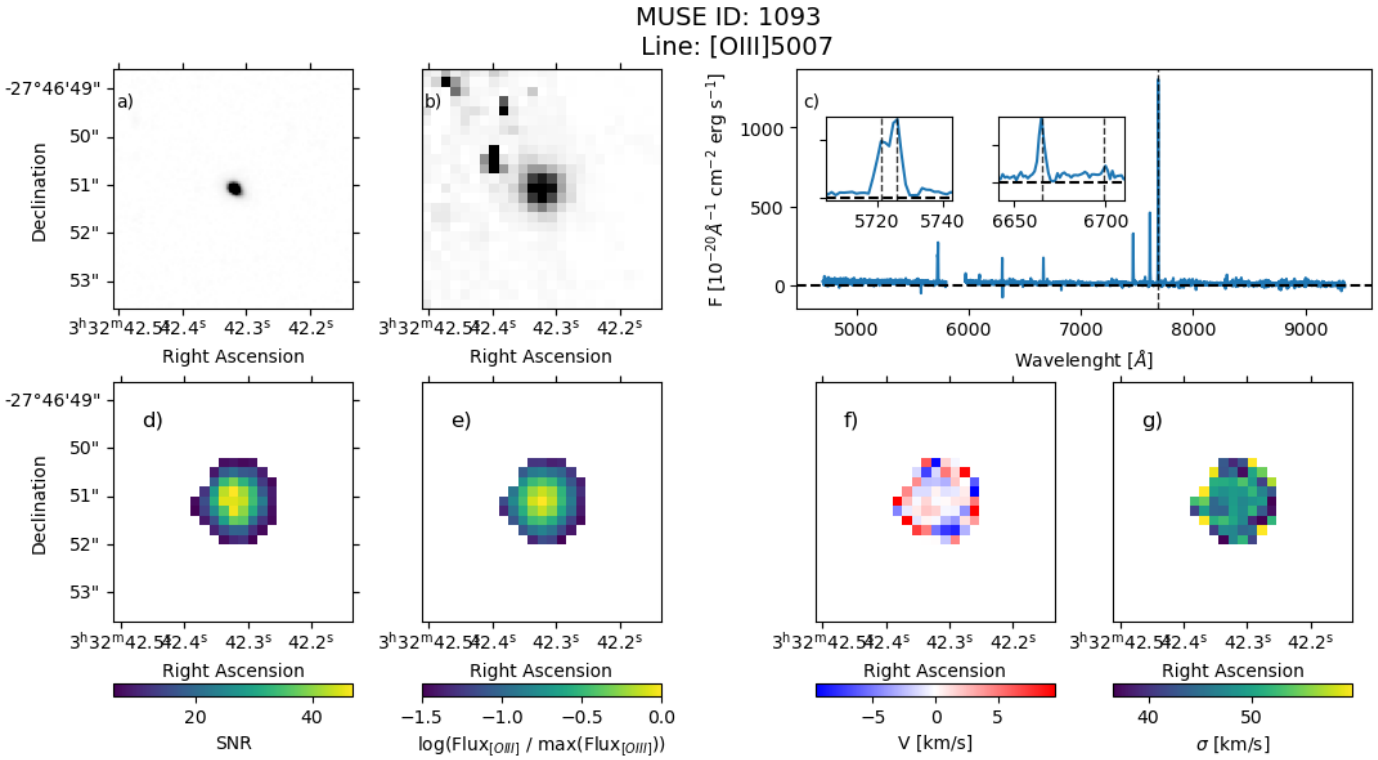

Fig. B.1. Same as Fig. 3, but for MUSE ID galaxy 1093.

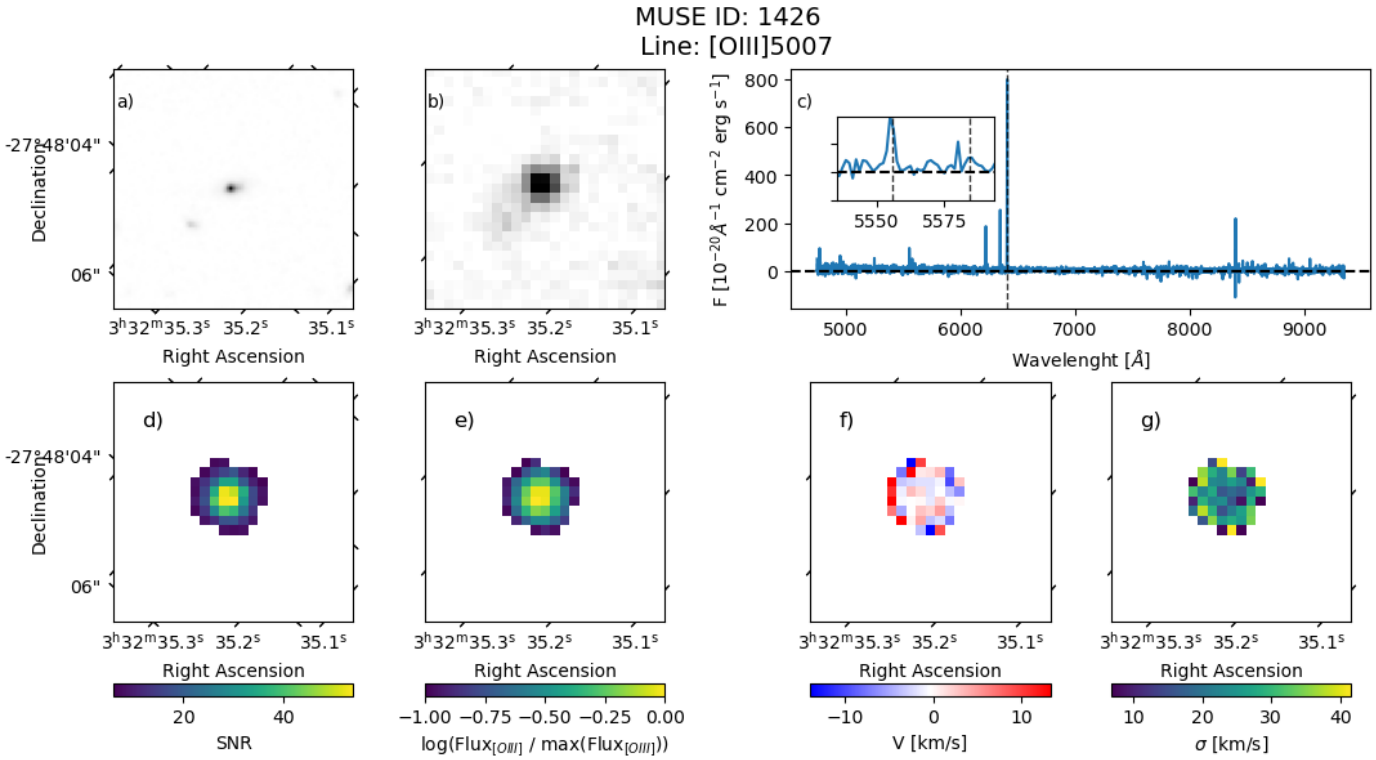

Fig. B.2. Same as Fig. 3, but for MUSE ID galaxy 1426.

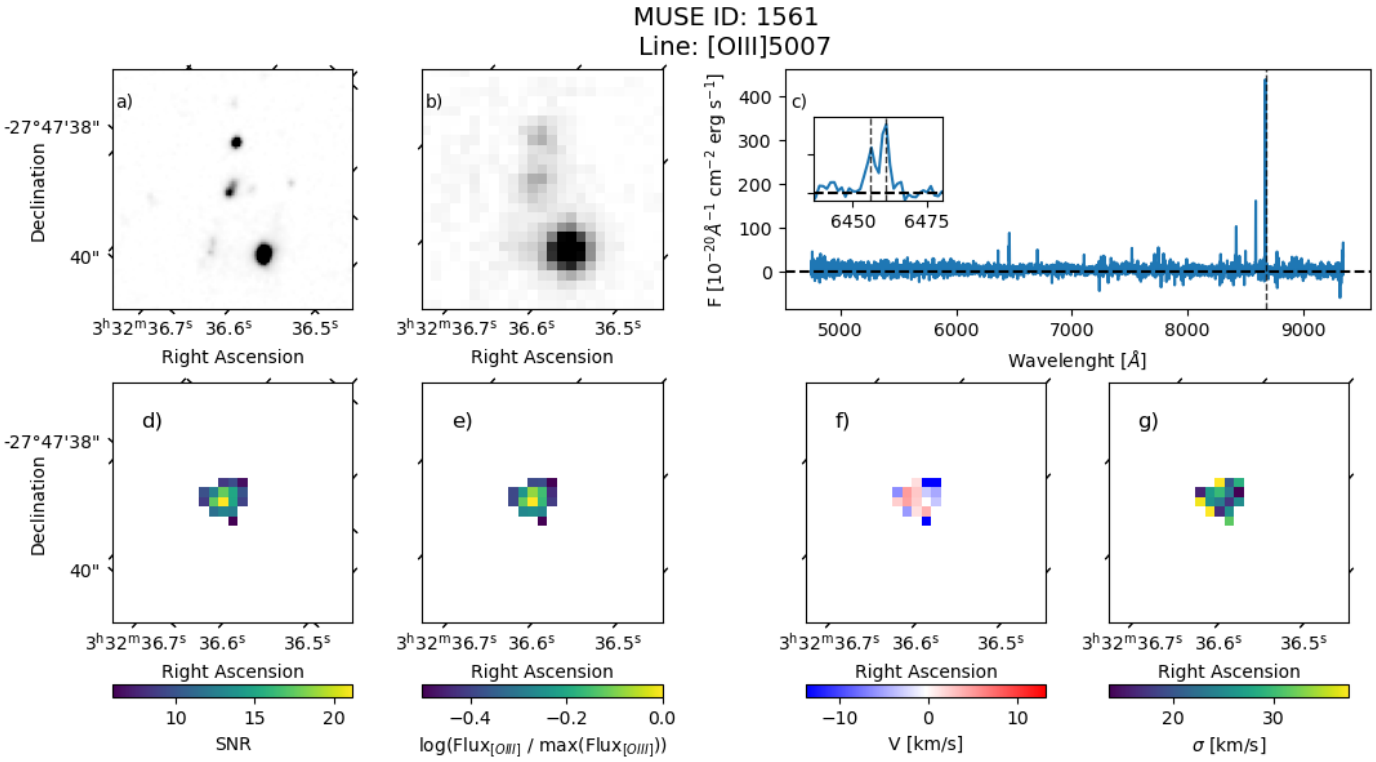

Fig. B.3. Same as Fig. 3, but for MUSE ID galaxy 1561.

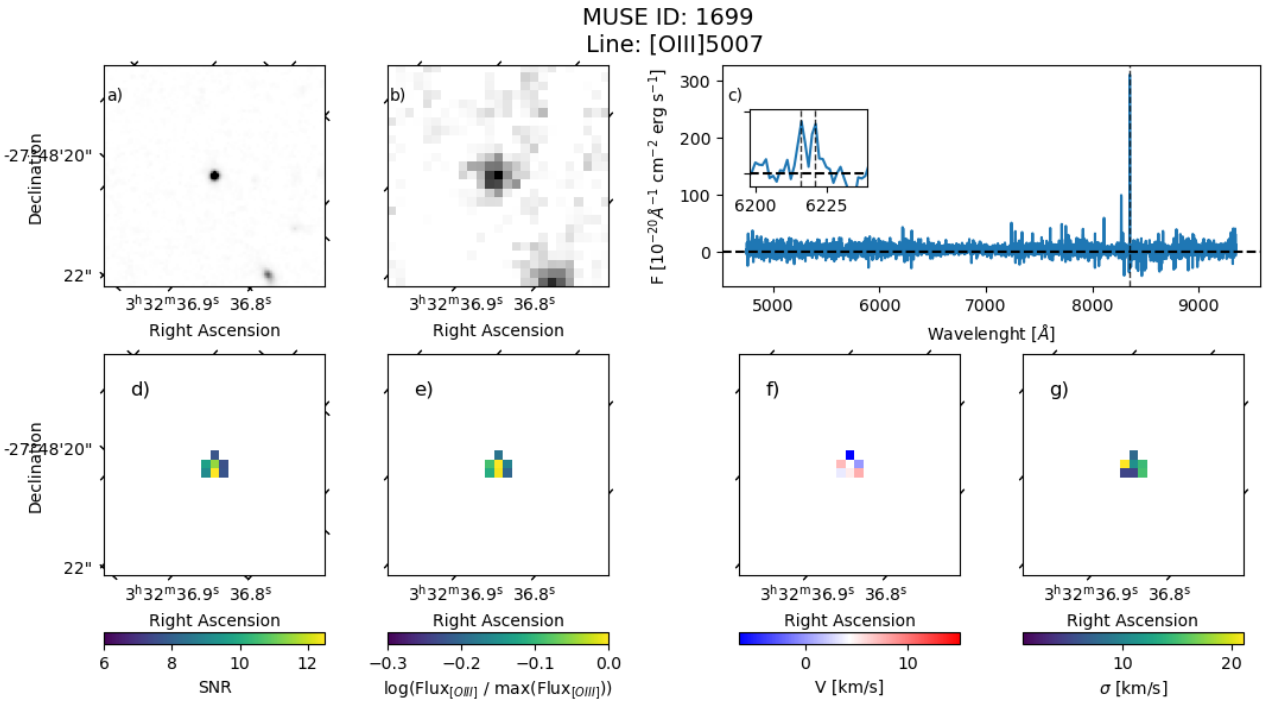

Fig. B.4. Same as Fig. 3, but for MUSE ID galaxy 1699.

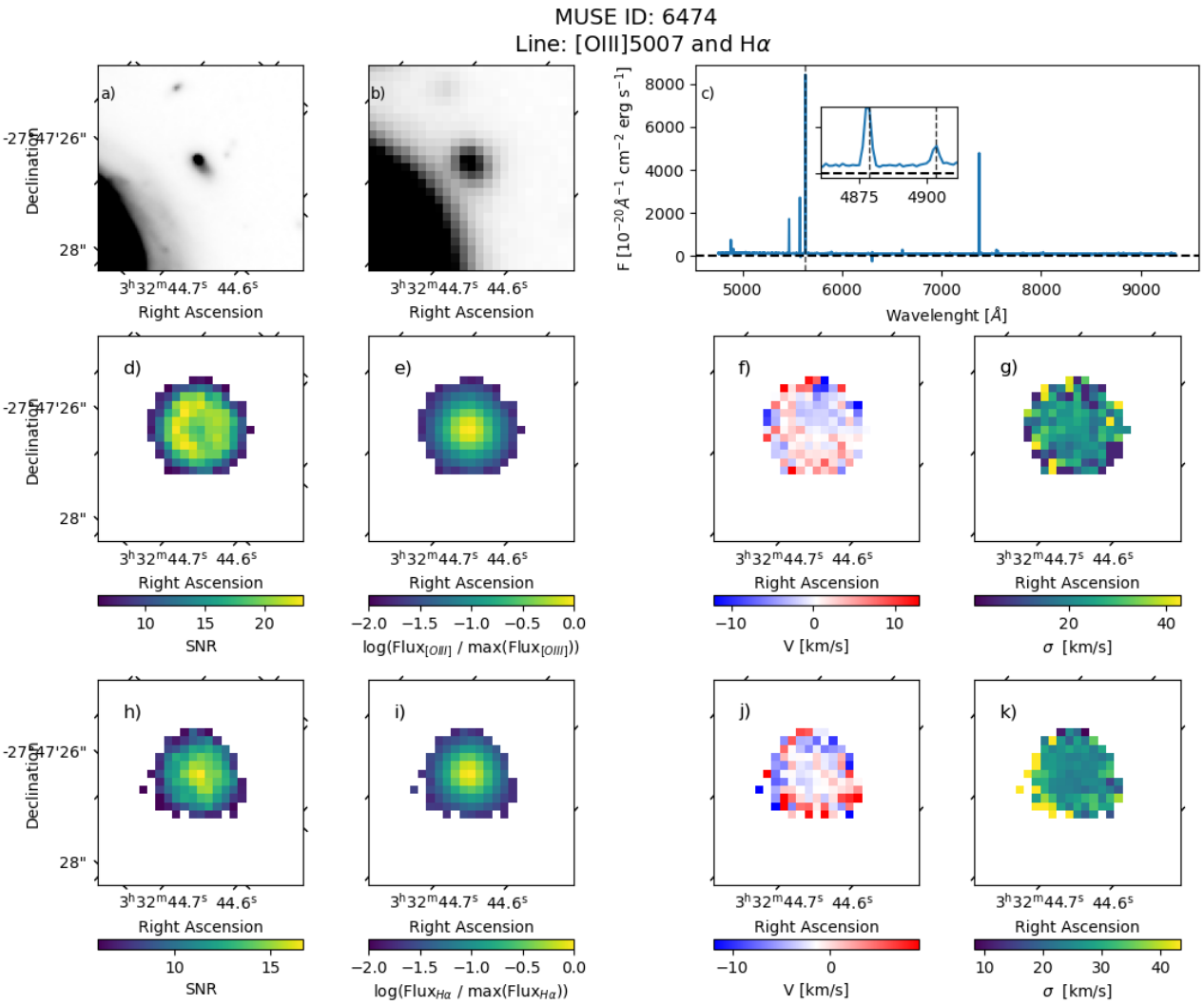

Fig. B.5. Same as Fig. 3, but for MUSE ID galaxy 6474.

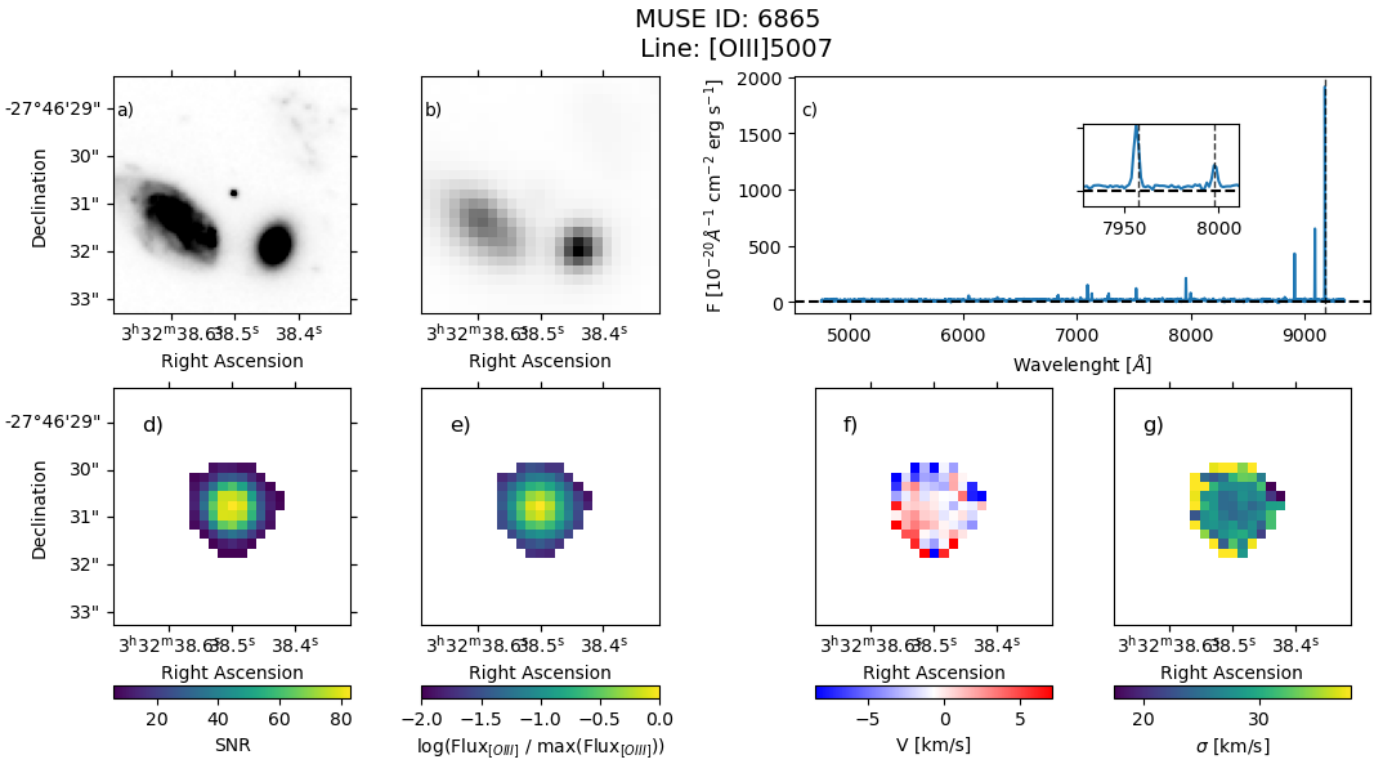

Fig. B.6. Same as Fig. 3, but for MUSE ID galaxy 6865.

Appendix C: Line fluxes of the EELG primary sample candidates

In this appendix, we show the fluxes and equivalent width measured with pyPlatefit for our EELG sample. Only lines with an S/N higher than three are included in the tables.

	Galaxy ID	91	891	895	2478	2532	6465	7373
Line	λ (Å)	F ($10^{-20}\frac{erg}{scm^2}$)	F ($10^{-20}\frac{erg}{scm^2}$)	F ($10^{-20}\frac{erg}{scm^2}$)	F ($10^{-20}\frac{erg}{scm^2}$)	F ($10^{-20}\frac{erg}{scm^2}$)	F ($10^{-20}\frac{erg}{scm^2}$)	F ($10^{-20}\frac{erg}{scm^2}$)
(1)	(2)	(3)	(4)	(5)	(6)	(7)	(8)	(9)
[OII]	3726.03	257 ± 7	...	...	...	...	94 ± 2	...
[OII]	3728.82	356 ± 5	...	...	...	...	125 ± 3	...
H11	3770.63	21 ± 5	...	...	...	...	...	...
H10	3797.90	41 ± 4	...	...	...	...	...	...
H9	3835.39	52 ± 3	...	1347 ± 34	...	...	...	...
[NeIII]	3868.75	277 ± 8	...	6342 ± 8	135 ± 4	38 ± 4	54 ± 2	...
[HeI]	3888.65	132 ± 3	4266 ± 8	3298 ± 28	48 ± 2	...	...	...
H8	3889.05	134 ± 5	4213 ± 8	3264 ± 28	47 ± 2	...	...	...
[NeIII]	3967.46	95 ± 3	3588 ± 11	2940 ± 9	...	...	...	...
Hϵ	3970.07	98 ± 6	4016 ± 9	3209 ± 11	49 ± 4	...	...	...
Hδ	4101.74	196 ± 4	5757 ± 6	4515 ± 27	92 ± 4	...	...	...
Hγ	4340.47	354 ± 5	9956 ± 7	8167 ± 18	142 ± 2	...	62 ± 5	...
[OIII]	4363.21	91 ± 5	1609 ± 8	1399 ± 12	39 ± 4	...	...	...
Hβ	4861.33	779 ± 8	21673 ± 10	18180 ± 16	162[a]	109 ± 3	102 ± 9	31 ± 2
[OIII]	4958.91	1364 ± 3	32476 ± 16	30788 ± 5	583 ± 3	198 ± 2	158 ± 7	...
[OIII]	5006.84	4099 ± 6	95521 ± 16	92673 ± 17	2065 ± 3	492 ± 3	668 ± 6	34 ± 1
[HeI]	5875.67	...	2387 ± 13	2119 ± 6	...	...	...	...
[OI]	6300.30	...	851 ± 7	851 ± 8	...	...	...	...
Hα	6562.82	...	67942 ± 15	57500 ± 9	...	...	...	102 ± 2
[NII]	6583.41	...	1356 ± 8	1404 ± 11	...	...	...	...
[SII]	6716.47	...	3614 ± 8	3302 ± 10	...	...	...	...
[SII]	6730.85	...	2638 ± 9	2463 ± 5	...	...	...	...
[ArIII]	7135.78	...	1302 ± 6	1464 ± 10	...	...	...	...

Table C.1. Observed line fluxes for the primary sample. (1) Emission line; (2) rest-frame wavelength; (3) observed line fluxes for ID 91; (4) observed line fluxes for ID 891; (5) observed line fluxes for ID 895; (6) observed line fluxes for ID 2478; (7) observed line fluxes for ID 2532; (8) observed line fluxes for ID 6465; (9) observed line fluxes for ID 7373. [a] Uncertain value.

Appendix D: Line fluxes of the EELG extended sample candidates

Here, we present the fluxes and equivalent width measured with pyPlatefit for our extended sample. Only lines with an S/N higher than three are included in the tables.

	Galaxy ID	1093	1426	1561	1699	6474	6865
Line	λ (Å)	F ($10^{-20}\frac{erg}{scm^2}$)	F ($10^{-20}\frac{erg}{scm^2}$)	F ($10^{-20}\frac{erg}{scm^2}$)	F ($10^{-20}\frac{erg}{scm^2}$)	F ($10^{-20}\frac{erg}{scm^2}$)	F ($10^{-20}\frac{erg}{scm^2}$)
(1)	(2)	(3)	(4)	(5)	(6)	(7)	(8)
[MgII]	2795.53	...	...	...	...	...	57 ± 3
[OII]	3726.03	673 ± 6	107 ± 4	164 ± 4	107 ± 3	...	132 ± 3
[OII]	3728.82	981 ± 6	274 ± 4	262 ± 4	102 ± 3	...	126 ± 3
H11	3770.63	...	...	...	...	...	61 ± 3
H10	3797.90	...	...	...	...	...	78 ± 3
H9	3835.39	...	...	...	...	...	102 ± 2
[NeII]	3868.75	...	175 ± 3	135 ± 4	52 ± 3	...	382 ± 2
[HeI]	3888.65	...	98 ± 3	...	...	...	214 ± 2
H8	3889.05	...	112 ± 4	63 ± 4	...	...	220 ± 2
[NeII]	3967.46	185 ± 6	...	...		...	166 ± 3
Hϵ	3970.07	243 ± 7	93 ± 4	...		...	222 ± 4
Hδ	4101.74	489 ± 8	154 ± 4	103 ± 5	55 ± 4	...	347 ± 3
Hγ	4340.47	620 ± 7	276 ± 4	175 ± 5	...	2260 ± 7	659 ± 3
[OIII]	4363.21	75 ± 6	...	...	...	605 ± 6	208 ± 2
Hβ	4861.33	1347 ± 9	626 ± 4	352 ± 6	221 ± 5	5023 ± 6	1453 ± 3
[OIII]	4958.91	1807 ± 7	771 ± 3	484 ± 4	309 ± 4	8562 ± 7	2054 ± 2
[OIII]	5006.84	5364 ± 9	2485 ± 5	1450 ± 6	905 ± 5	26044 ± 8	6276 ± 3
[HeI]	5875.67	135 ± 7	53 ± 3	...	...	543 ± 7	...
[OI]	6300.30	...	...	....	...	156 ± 6	...
Hα	6562.82	...	...	....	...	15343 ± 7	...
[NII]	6583.41	...	...	....	...	214 ± 6	...
[SII]	6716.47	...	...	...	...	588 ± 6	...
[SII]	6730.85	...	...	...	...	444 ± 6	...
[ArIII]	7135.78	...	...	...	...	293 ± 7	...

Table D.1. Same as Table C.1, but for the extended sample. [a] Uncertain value.